UNIVERSITY *of York*

This is a repository copy of *A Novel Winding Switching Control Strategy of a Consequent-Pole Ferrite-PM Hybrid-Excited Machine for Electric Vehicle Application*.

White Rose Research Online URL for this paper:
https://eprints.whiterose.ac.uk/192672/

Version: Accepted Version

White Rose
university consortium
Universities of Leeds, Sheffield & York

eprints@whiterose.ac.uk
https://eprints.whiterose.ac.uk/

A Novel High-Order-Harmonic Winding Design Method for Vernier Reluctance Machine with DC Coils across Two Stator Teeth

Journal:	*Transactions on Industrial Electronics*
Manuscript ID	21-TIE-1062.R1
Manuscript Type:	Regular paper
Manuscript Subject:	Machines and Drives
Keywords:	Vernier reluctance machine, High-order-harmonic winding, Torque density improvement
Are any of authors IEEE Member?:	Yes
Are any of authors IES Member?:	Yes

SCHOLARONE™
Manuscripts

A Novel High-Order-Harmonic Winding Design Method for Vernier Reluctance Machine with DC Coils across Two Stator Teeth

Xing Zhao, *Member, IEEE*, Sigao Wang, Shuangxia Niu, *Senior Member, IEEE,* Weinong Fu, Xiaodong Zhang

Abstract—**Vernier reluctance machine (VRM) with DC field coils in stator is a competitive rare-earth-free design for variable-speed industrial applications due to its robust structure and controllable excitation, while its torque density is relatively disadvantageous. To address this issue, this paper proposes a new armature winding design method for VRM with DC field coils across two stator teeth. The key is to break the traditional winding design principle based on the flux modulation effect of fundamental DC field harmonic, and instead, reconstruct a novel harmonic winding to enhance the utilization factor of the modulated high-order DC field harmonics arising from the unique magnetomotive force distribution of DC field coils across two stator teeth. By this means, the torque density can be improved by 75.6% compared to the existing counterpart. In this paper, the machine structure and operation principle are introduced, with emphasis on the high-order DC field harmonics distribution rule and its influence on the armature winding design. By finite element design and optimization, a comparative study is performed to evaluate the electromagnetic performance of VRMs using two different winding configurations with variable slot pole combinations. A prototype is fabricated and tested, and the results agree well with finite element analysis, which verifies the feasibility and advantages of the proposed winding design method.**

Index Terms—**Flux modulation, high-order-harmonic winding, torque density, Vernier reluctance machine.**

I. Introduction

DUE to a limited resource of rare-earth PM material and the associated price fluctuation, the system cost of permanent magnet machines show a significant growth in the recent years. Therefore, developing new reluctance machines without using permanent magnets (PM) becomes a hot research topic [1-4]. The synchronous reluctance machine is a promising non-PM candidate which share the same stator design and drive circuit with traditional PM machines, but its torque density and power factor are unsatisfactory [5-6]. Besides, the mechanical strength of magnetic barrier rotor is relatively weak, which restricts its industry applications. Some other types of reluctance machines employing a doubly salient structure present better mechanical robustness, including the switched reluctance machine (SRM), doubly-fed doubly salient machine (DF-DSM) and variable flux reluctance machine (VFRM). The state of art of these doubly salient topologies is provided as follows.

SRM has been well investigated in literature for many years

and thus its design, modeling and control methods are relatively mature [7-9]. Nevertheless, the industrial applications of SRM are still limited. On one hand, the torque ripple of SRM is serve due to half-period-conducting principle, which leads to distinct mechanical vibration and noise. On the other hand, the drive circuit for SRM is an asymmetry half-bridge converter, thus the commercialized inverter package cannot be applied. To address this issue, a six-phase SRM with armature winding connected with diodes, is proposed to enable inverter driven feature [10], while the feasibility of slot pole design is reduced.

DF-DSM shares a similar stator and rotor structure with SRM but equipped with extra DC field coils in stator core. Benefiting from the DC field coils, an alternating excitation flux linkage is established, which enables DF-DSM to work in a whole period. Hence, DF-DSM can be driven by a universal inverter package [11-12]. The main issue of DF-DSM that limits its applications is the large torque ripple, caused by the asymmetrical magnetic circuit [13], rich even-order flux harmonics and the associated distorted back electromotive force (EMF) [14-15].

VFRM can be considered as a special DF-DSM by changing the layout of DC coils to create a more uniform magnetomotive force and thus enables more flexible slot pole designs [16-17]. Especially, VFRM with odd rotor poles in unit machine design shows distinctly reduced torque ripple compared to DF-DSM, due to symmetrical magnetic circuit, eliminated even-order flux harmonics and constant phase inductance [18]. Considering the inverter-driven feature and low torque ripple, VFRM is a good non-PM candidate for industrial applications. The bottleneck of VFRM is low torque density. In the recent years, it is revealed VFRM operates based on the flux modulation principle and thus can be referred as Vernier reluctance machine (VRM) [19-20]. To improve the torque density of VRM, integrated armature and field current control can be applied using zero-sequence current injection to eliminate the space conflict between AC coils and DC coils [21-23]. However, the dual inverter should be adopted, which increases the complexity of drive circuit.

VRMs with DC coils across two stator teeth is an emerging non-PM candidate. Compared to DF-DSM, it has symmetrical magnetic circuit and sinusoidal back EMF, which contributes to reduced torque ripple [24-26]. Compared to the traditional VRMs using full DC coils, it shows comparable torque density but with reduced DC coils and the associated DC copper loss. In general, VRMs with DC coils across two stator teeth, can be a potential non-PM topology that integrates both small torque ripple and acceptable efficiency, while its torque density (about 5kNm/m^3 [27-28]) needs to be further improved for industrial applications. The reasons for low torque density of existing VRM structures include: (1) The flux linkage in each armature coil is biased, thus the stator core utilization factor is relatively

low. (2) Some working harmonics in the air gap are not fully utilized when using the traditional winding design method.

In this paper, a novel armature winding design method will be proposed to improve the torque density of VRMs with DC coils across two stator teeth. The key is to break the traditional winding design principle based on the flux modulation effect of fundamental harmonic of excitation source, and instead, design a novel high-order harmonic winding according to the unique distribution of magnetomotive force excited by DC coils across two stator teeth, thus achieve enhanced flux modulation effect to boost torque density. The rest of paper is organized as follows. In Section II, the machine structure, armature winding designs, and operation principle are introduced by harmonics analysis based on a magnetomotive-force-permeance analytical model. In Section III, the Genetic Algorithm (GA) is used to perform multi-objective design and optimization for VRMs considering different winding design methods and slot pole combinations. In Section IV, the optimal cases are comprehensively compared in terms of the flux linkage, back EMF, torque performance, loss, efficiency, power factor, as well as radial magnetic force. In Section V, a prototype is fabricated, and the experiments are performed for the feasibility verification of proposed solution. Finally, some conclusions are drawn in Section VI.

II. MACHINE STRUCTURE AND WORKING PRINCIPLE

A. Machine structure and winding designs

The configuration of Vernier reluctance machine (VRM) to be analyzed is presented in Fig.1. There are 12 stator slots and 11 rotor poles. The rotor consists of iron core only and hence shows good mechanical robustness. There are two groups of windings in the stator slots, namely DC field winding and AC armature winding, respectively. The DC field coils are wound across every two stator teeth, which will produce abundant field harmonics including the fundamental field harmonic and other high order components. How to design an AC armature winding to achieve the highest utilization factor of DC field harmonics, becomes an interesting topic in this VRM topology.

Two feasible designs of AC armature winding are discussed in this paper. One is the traditional winding configuration that is designed based on the flux modulation effect of fundamental DC field harmonic, which can be expressed as

$$PPN_a = \left| N_p - N_r \right| \tag{1}$$

where PPN_a is the pole pair number (PPN) of AC armature winding, N_r is the number of rotor salient poles, and N_p is the PPN of fundamental harmonic of DC field excitation. The other new armature winding design is proposed according to the flux modulation effect of high-order DC field harmonics, especially the rich components modulated from the third-order DC field harmonic component excited by the unique distribution of DC field coils across two stator teeth, which will be expanded in the Part B. The design principle of proposed high-order-harmonic armature winding can be expressed as

$$PPN_a = \left| 3N_p - N_r \right| \tag{2}$$

Using the case of 12 stator slots and 11 rotor pole pairs, detail connections of two winding designs based on equations (1) and (2) are presented in Fig. 2(a) and Fig. 2(b), respectively.
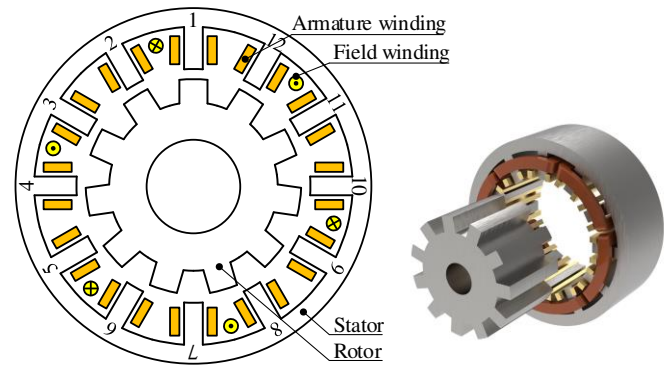
Fig. 1. Structure of 12/11 VRM with DC field coils across two stator teeth.

(a)

(b)
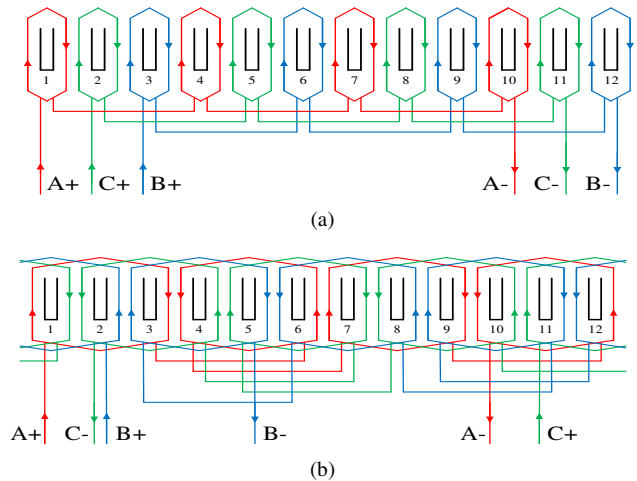
Fig. 2. Connections of AC armature winding. (a) The traditional fundamental-harmonic design. (b) The proposed high-order-harmonic design.

B. Distribution rule of DC field harmonics

To provide a deep understanding of the proposed winding design method, it is necessary to analyze the distribution rule of DC field harmonics in air gap. In this paper, a simple air-gap magnetomotive force (MMF) and permeance analytical model is utilized to calculate the air-gap flux density and determine the harmonics distribution [27].
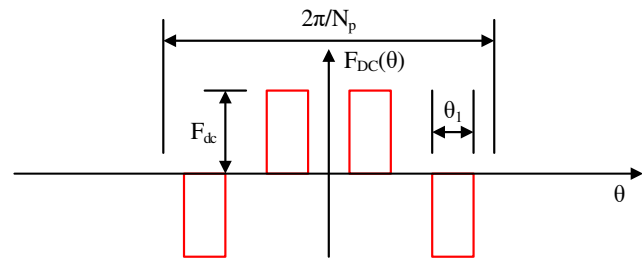
Fig. 3. MMF waveform generated by DC field excitation.

Fig. 3 presents the MMF waveform with respective to mechanical angle generated by DC field coils across two stator teeth. The amplitude of MMF waveform under every stator tooth is the same due to magnetic circuit symmetry, and the polarity of MMF is changed every two teeth. Therefore, it can be further expanded by means of Fourier Series as

$$\begin{cases} F_{DC}(\theta) = \sum_{n=1}^{+\infty} F_n \cos(nN_p\theta) \\ F_n = \frac{4F_{dc}}{n\pi} \sin\left(n\frac{N_p}{2}\theta_1\right)\left[\cos\left(\frac{n\pi}{4}\right) - \cos\left(\frac{3n\pi}{4}\right)\right] \end{cases} \quad (3)$$

where F_{dc} is the equivalent MMF of DC field current, θ is the mechanical angle, θ_1 is the mechanical angle of the stator tooth.
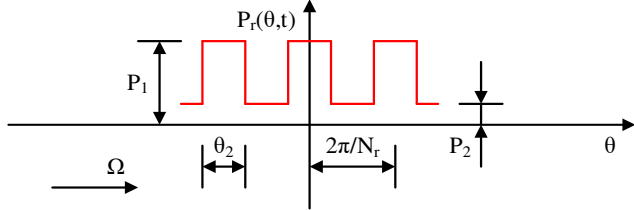

Fig. 4. Rotor permeance waveform.

Fig. 4 presents the rotor permeance that is modulated by rotor slots and salient poles, and it can be expanded as

$$\begin{cases} P_r(\theta,t) = \frac{P_0}{2} + \sum_{k=1}^{+\infty} P_k \cos[kN_r(\theta - \omega_{me}t)] \\ P_0 = 2P_2 + \frac{(P_1 - P_2)\theta_2 N_r}{\pi} \\ P_k = \frac{2}{k\pi}(P_1 - P_2)\sin\left(kN_r\frac{\theta_2}{2}\right) \end{cases} \quad (4)$$

where P_1 is the permeance of rotor salient poles, and P_2 is the permeance of rotor slots, N_r is the number of rotor salient poles, ω_{me} is the mechanical angular speed of the rotor, θ_2 is the mechanical angle of the rotor salient pole.

The air-gap flux density can be deduced by multiplying (3) and (4), and be further expressed as:

$$B_r(\theta,t) = F_{DC}(\theta)P_r(\theta,t) = \sum_{n=1}^{+\infty}\sum_{k=-\infty}^{+\infty} \frac{F_n P_{|k|}}{2}\cos(nN_p\theta + kN_r\theta - kN_r\omega_{me}t) \quad (5)$$

TABLE I
DISTRIBUTION OF AIR-GAP DC FIELD HARMONICS

Group Number	Pole Pair Number	Rotating Speed
I	$N_p n$	0
II	$N_p n + N_r k$	$\frac{N_r k}{N_p n + N_r k}\omega_{me}$
III	$\lvert N_p n - N_r k\rvert$	$\frac{N_r k}{\lvert N_p n - N_r k\rvert}\omega_{me}$

The PPN of each harmonic component and its rotation speed can be summarized in Table I based on the result in (5). There are three groups of modulated air-gap harmonics. The harmonic components in Group I are corresponding to the case when $k=0$. They are not modulated by the rotor salient poles and instead established directly from DC field current. They have zero rotation speed, which means they cannot be utilized as working harmonics. The harmonic components in Group II are related to the cases when k is positive number, and the Group III is corresponding to the cases when k is negative. The harmonics in Group II and III are modulated by the rotor salient poles, and some of them can be utilized as working harmonics.

C. Selection of the main working harmonics

For the traditional design method of AC armature winding,

the main working harmonic is selected as the component which is modulated from the fundamental DC field harmonic (PPN of $\lvert N_p - N_r\rvert$, with n=1, k=-1), while for the proposed design method, the main working harmonic is determined as the one modulated from the third-order DC field harmonic (PPN of $\lvert 3N_p - N_r\rvert$, with n=3, k=-1). Further, to explain the reasonability of the proposed high-order-harmonic winding design method, the ratio of flux density amplitudes of the above two working harmonics can be derived out by (5) and expressed as follows

$$\left|\frac{B_{(1,-1)}}{B_{(3,-1)}}\right| = \left|\frac{F_1 P_{|-1|}}{F_3 P_{|-1|}}\right| =$$

$$\left|\frac{\frac{4F_{dc}}{\pi}\sin\left(\frac{N_p}{2}\theta_1\right)\left[\cos\left(\frac{\pi}{4}\right)-\cos\left(\frac{3\pi}{4}\right)\right]}{\frac{4F_{dc}}{3\pi}\sin\left(3\frac{N_p}{2}\theta_1\right)\left[\cos\left(\frac{3\pi}{4}\right)-\cos\left(\frac{9\pi}{4}\right)\right]}\right| = \left|\frac{3\sin\left(\frac{N_p}{2}\theta_1\right)}{\sin\left(\frac{3N_p}{2}\theta_1\right)}\right| \quad (6)$$

where $B_{(1,-1)}$ and $B_{(3,-1)}$ refer to the flux density amplitude of the main working harmonic in the traditional design method and the proposed design method, respectively. It is interesting to find that the result is related to the PPN of DC field excitation N_p and the mechanical angle of stator tooth θ_1, but independent of the number of rotor salient poles N_r.

Assuming the mechanical angle of stator tooth is in close to that of the adjacent stator slot opening, which means

$$\theta_1 \approx \frac{\pi}{4N_p} \quad (7)$$

By substituting (7) into (6), the ratio between two main working harmonics can be calculated as

$$\left|\frac{B_{(1,-1)}}{B_{(3,-1)}}\right| = \left|\frac{3\sin\left(\frac{N_p}{2}\theta_1\right)}{\sin\left(\frac{3N_p}{2}\theta_1\right)}\right| \approx 1.24 \quad (8)$$

The result in (8) indicates, regardless of the number of the rotor salient poles, the ratio between $B_{(1,-1)}$ and $B_{(3,-1)}$ is always in close to 1.24. This is because the flux density of main working harmonics is mainly determined by the fundamental waveform of DC field excitation. Because of the unique distribution of DC field coils across two stator teeth in the proposed VRMs, the flux density amplitude of the $\lvert N_p - N_r\rvert$ order harmonic and the $\lvert 3N_p - N_r\rvert$ order harmonic are very close, which provides more design feasibility in the proposed VRMs to reselect the main working harmonic and boost torque density. Specifically, we propose a new $\lvert 3N_p - N_r\rvert$ winding design method to reselect the high-order harmonics as the main working harmonics in VRM structures. Because the reselected main working harmonic has higher rotating speed, enhanced back EMF and torque generation can be achieved. The detail analysis of harmonics contribution on back EMF will be expanded in the Part E. Overall, the proposed winding design method breaks the traditional $\lvert N_p - N_r\rvert$ winding design principle based on the flux modulation theory of fundamental harmonic, and thus provides more feasible slot pole combinations and winding design choices.

It should be pointed out, when the similar MMF analysis is applied to VRMs with DC field coils fully wound on every stator tooth, the ratio between $B_{(1,-1)}$ and $B_{(3,-1)}$ can be derived

out as 3. In other words, the flux density amplitude of $|3N_p\text{-}N_r|$ order harmonic is much smaller compared to that of $|N_p - N_r|$ order harmonic. Hence, the proposed winding design method is not recommended for VRMs with full DC field coils.

TABLE II
PPN OF ARMATURE WINDING USING DIFFERENT DESIGNS

N_{slot}	N_r	PPN of the traditional $|N_p - N_r|$ winding	PPN of the proposed $|3N_p - N_r|$ winding
12	11	8	2
12	10	7	1
12	8	5	1
12	7	4	2
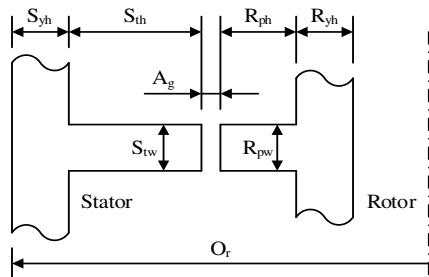
Fig. 5. Notations of dimensional parameters.

TABLE III
DIMENSION PARAMETERS OF INITIAL DESIGN

Item	Notation	Value
Stack length (mm)	L_{st}	50
Outer radius (mm)	O_r	70
Stator tooth width (mm)	S_{tw}	8
Stator tooth height (mm)	S_{th}	20
Stator yoke height (mm)	S_{yh}	9
Air gap length (mm)	A_g	0.5
Rotor pole height (mm)	R_{ph}	10
Rotor yoke height (mm)	R_{yh}	20
Rotor pole width (mm)	R_{pw}	9
Number of turns of DC field coil	N_{DC}	126
Number of turns of AC armature coil	N_{AC}	96
Rotation speed (rpm)	S_{pd}	900
DC current (A)	I_{DC}	5.34

D. Example cases and initial FEA validation

This part shows the example cases with finite element models to validate the above-mentioned analysis of airgap harmonic distribution. In the example cases, four slot pole designs with N_{slot}/N_r of 12/11, 12/10, 12/8 and 12/7 are considered to validate the flux density ratio between $B_{(1,-1)}$ and $B_{(3,-1)}$. Based on (1) and (2), the PPN of corresponding armature winding in four cases using two different design methods are presented in Table II. Some common dimension parameters of four initial designs are labeled in Fig. 5, and their values are given in Table III. The calculated airgap harmonics distribution of four cases are presented in Fig. 6, including the flux density waveforms and the associated harmonics spectrum obtained by Fast Fourier Analysis. The main working harmonic to be used in two different winding configurations are further highlighted in marked in red and blue color, respectively.
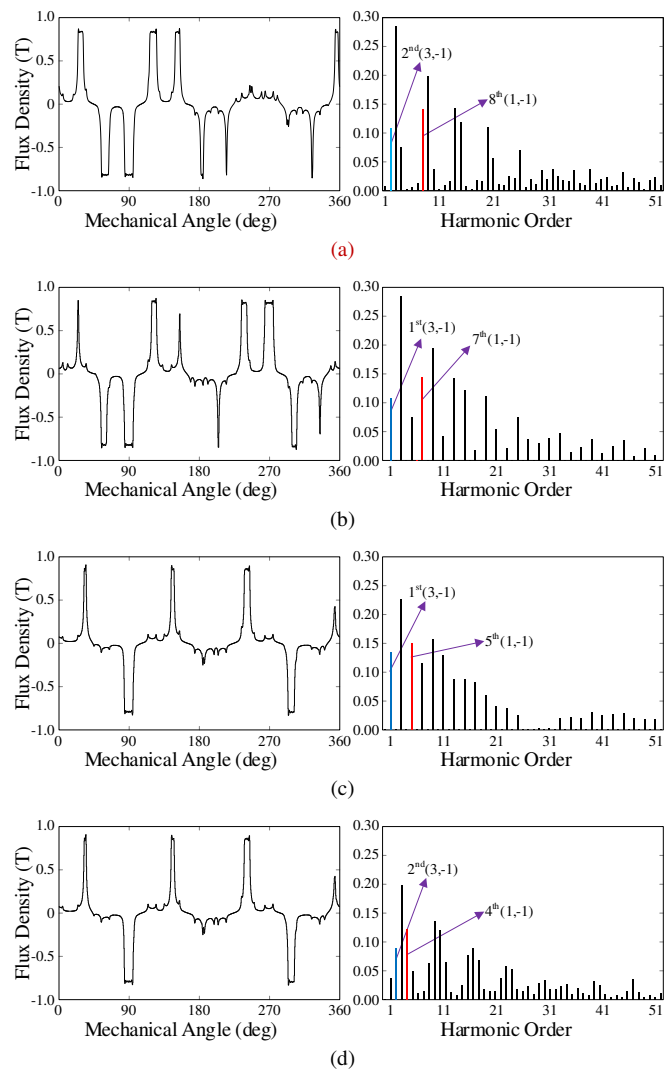
Fig. 6. Air-gap field and harmonics of VRMs. (a) 11 rotor salient poles. (b) 10 rotor salient poles. (c) 8 rotor salient poles. (d) 7 rotor salient poles.

With their flux density amplitudes listed in Table IV, it can be found that the ratio between $B_{(1,-1)}$ and $B_{(3,-1)}$ is 1.30 for 12/11 case, 1.32 for 12/10 case, 1.12 for 12/8 case, 1.39 for 12/7 case, respectively. This basically agrees with the result from theoretical analysis in (8) considering the mechanical angle of stator tooth is not exactly the same with slot opening angle.

TABLE IV
AMPLITUDES OF MAIN WORKING HARMONICS

N_{slot}	N_r	$B_{(1,-1)}$ (T)	$B_{(3,-1)}$ (T)	$\left\|\dfrac{B_{(1,-1)}}{B_{(3,-1)}}\right\|$
12	11	0.142	0.109	1.31
12	10	0.144	0.109	1.32
12	8	0.150	0.134	1.12
12	7	0.123	0.089	1.39

E. Quantitative analysis of harmonics contribution

The following part gives the analytical relation between open-circuit back EMF and working harmonics with two winding designs. The amplitude of back EMF is in direct proportion to torque production if core saturation is not considered, and the back EMF can be expressed as:

TABLE V
OPEN-CIRCUIT BACK EMF CONTRIBUTION FROM DIFFERENT HARMONICS IN 12/11/8 MODEL

Order	(n,k)	B_n (T)	ω_n	k_{pn}	k_{dn}	k_{wn}	$B_n\omega_n k_{wn}$	$\Sigma B_n\omega_n k_{wn}$
2	(3,-1)	0.1093	$11\omega_{me}/2$	0.5	0	0	0	
4	(5,-1)	0.0755	$11\omega_{me}/4$	0.866	1	0.866	$0.1798\omega_{me}$	
8	(1,-1)	0.1419	$11\omega_{me}/8$	0.866	1	0.866	$0.1690\omega_{me}$	
10	(7,-1)	0.0376	$11\omega_{me}/10$	0.5	0	0	0	
14	(-1,-1)	0.1433	$11\omega_{me}/14$	-0.5	0	0	0	
16	(9,-1)	0.007	$11\omega_{me}/16$	-0.866	1	-0.866	$-0.004\omega_{me}$	$0.3072\omega_{me}$
20	(-3,-1)	0.1096	$11\omega_{me}/20$	-0.866	1	-0.866	$-0.0522\omega_{me}$	
22	(11,-1)	0.0114	$11\omega_{me}/22$	-0.5	0	0	0	
26	(-5,-1)	0.0704	$11\omega_{me}/26$	0.5	0	0	0	
28	(13,-1)	0.0198	$11\omega_{me}/28$	0.866	1	0.866	$0.0067\omega_{me}$	
32	(-7,-1)	0.0370	$11\omega_{me}/32$	0.866	1	0.866	$0.0110\omega_{me}$	

TABLE VI
OPEN-CIRCUIT BACK EMF CONTRIBUTION FROM DIFFERENT HARMONICS IN 12/11/2 MODEL

Order	(n,k)	B_n (T)	ω_n	k_{pn}	k_{dn}	k_{wn}	$B_n\omega_n k_{wn}$	$\Sigma B_n\omega_n k_{wn}$
2	(3,-1)	0.1093	$11\omega_{me}/2$	1	1	1	$0.6010\omega_{me}$	
4	(5,-1)	0.0755	$11\omega_{me}/4$	0	0	0	0	
8	(1,-1)	0.1419	$11\omega_{me}/8$	0	0	0	0	
10	(7,-1)	0.0376	$11\omega_{me}/10$	1	1	1	$0.0413\omega_{me}$	
14	(-1,-1)	0.1433	$11\omega_{me}/14$	-1	1	-1	$-0.1125\omega_{me}$	
16	(9,-1)	0.007	$11\omega_{me}/16$	0	0	0	0	$0.5573\omega_{me}$
20	(-3,-1)	0.1096	$11\omega_{me}/20$	0	0	0	0	
22	(11,-1)	0.0114	$11\omega_{me}/22$	-1	1	-1	$-0.0057\omega_{me}$	
26	(-5,-1)	0.0704	$11\omega_{me}/26$	1	1	1	$0.0298\omega_{me}$	
28	(13,-1)	0.0198	$11\omega_{me}/28$	0	0	0	0	
32	(-7,-1)	0.0370	$11\omega_{me}/32$	0	0	0	0	

$$E_{phn} = \frac{4.44 D L T_{ph}}{60}\left(B_n k_{wn}\omega_n\right) \qquad (9)$$

where D is the diameter of the airgap circumference, L is the stack length, T_{ph} is the number of turns in a phase, E_{phn} is the amplitude of back EMF contributed by nth harmonic, B_n is the amplitude of nth harmonic, k_{wn} is the winding factor of nth harmonic, and ω_n is the rotation speed of nth harmonic.

To give a quantitative analysis between the proposed and traditional winding design, the open-circuit back EMF produced by each harmonic and their amplitude, rotation speed and winding factor are calculated and listed in Table V and Table VI, where k_{pn} and k_{dn} are pitch factor and distribution factor, respectively, using 12/11/8 and 12/11/2 cases as the examples. The harmonics with the order higher than 32 can be neglected as the amplitudes of flux density are too small.

Although $B_{(1,-1)}$ has relatively higher amplitude than $B_{(3,-1)}$, the corresponding rotation speed is much lower. Therefore, the model with proposed winding design has higher back EMF than traditional counterpart. The analytical ratio of back EMF between two winding designs is 1.814, which agrees with the FEA result of 1.934 (error = 6.86%). The results for 12/10, 12/8 and 12/7 cases are similar with that of 12/11 case. Due to relatively higher rotation speed, the main working harmonic in proposed winding design can contribute higher back EMF. Under the same dimensional parameters listed in Table III, the analytical and FEA results are summarized in Table VII. It can be found the analytical results well agree with FEA results.

In general, according to the flux modulation theory, the rotation speed of modulated harmonic is in inverse proportion to harmonic order. The lower order of working harmonic is, the higher rotation speed can be achieved, which means the higher back EMF and torque production can be obtained. This is the motivation of the proposed novel winding design method.

TABLE VII
ANALYTICAL AND FEA RESULTS OF OPEN-CIRCUIT BACK EMF RATIO

N_{slot}	N_r	Analytical	FEA	Error
12	11	1.814	1.9383	6.86%
12	10	3.139	2.8997	7.63%
12	8	2.9029	2.8430	2.06%
12	7	1.7848	1.7938	0.51%

III. DESIGN OPTIMIZATION

To show the effectiveness of the proposed winding design, machines with different rotor pole pairs are firstly optimized in this part and further comparatively evaluated in the Section IV. The genetic algorithm (GA) is combined with FEA method to fast search the optimal dimension parameters for four model with rotor pole pairs of 7, 8, 10, 11, respectively. The pole pair number of 9 is not included, because this case cannot form a three-phase design using the proposed winding design method. Four models are optimized using the same outer dimension and current density, with two objectives of the maximum average torque and minimum torque ripple. The flowchart of GA and FEA combined optimization process is shown in Fig. 7.
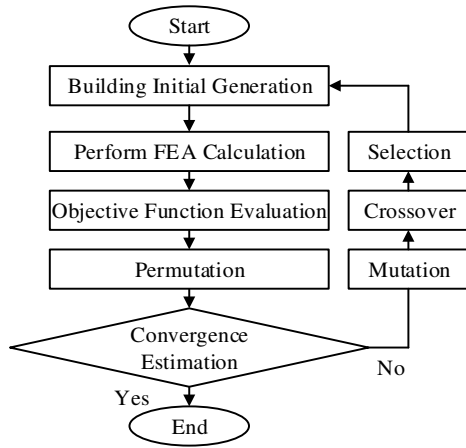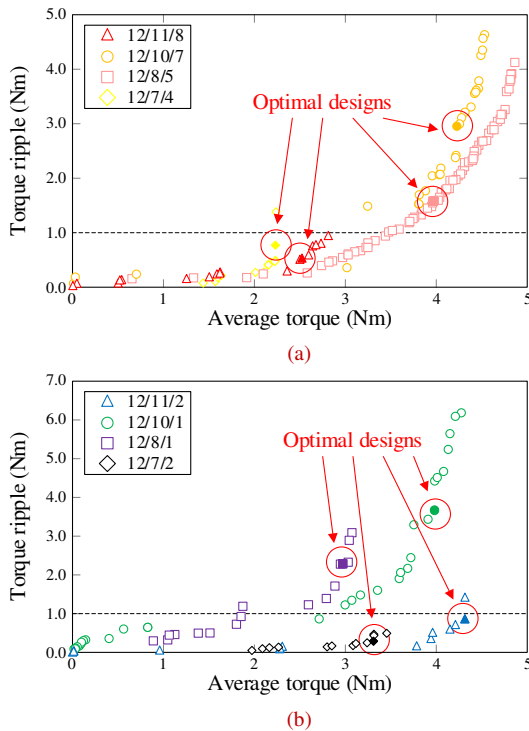
Fig. 7. Flow chart of FEA & GA optimization.

(a)

(b)

Fig. 8. Optimization results of the last generation (Pareto front). (a) Traditional $|N_p\text{-}N_r|$ winding design. (b) Proposed $|3N_p\text{-}N_r|$ winding design.

At first, to build the initial generation, a number of models are established with the same topology but different dimension parameters that are taken randomly within the given vibration range. Then, in the evaluation step, all the models are simulated under FEA to evaluate the torque performance. Further, in the selection process, a part of model is abandoned, and the rest of models are selected for the next step. Models with relatively poor torque performance has higher possibility to be abandoned. In the crossover step, the selected models exchange dimension parameters to form a new generation of models, and meanwhile, some dimensional parameters are mutated within a small range. After mutation, a new generation is built, which is supposed to have better average torque performance than the last generation. Finally, the difference between two adjacent generations will be estimated in the convergence setup, and the progress stops if the difference is smaller than the tolerance.

The common design parameters of four models include: the stack length of 50 mm, outer radius of 70 mm, air-gap length of 0.5 mm, rated speed of 900 rpm, current density of 6 A/mm² and slot filling factor of 0.6. After the optimization, the last generations of four models are given in Fig. 8. For each slot/pole/winding design, only one optimal model is selected, considering the tradeoff between average torque value and torque ripple. And their corresponding design data and torque performance index are listed in Table VIII and Table IX, respectively. It is shown, models using the proposed winding design method, can achieve higher maximum torque, which preliminarily proves its feasibility and technical advantage. The detail comparison of electromagnetic performance of the eight optimal models is presented in the next chapter.

TABLE VIII
OPTIMAL DIMENSIONAL PARAMETERS

	Traditional $|N_p\text{-}N_r|$ winding				Proposed $|3N_p\text{-}N_r|$ winding			
N_{slot}	12	12	12	12	12	12	12	12
N_r	11	10	8	7	11	10	8	7
PPN_a	8	7	5	4	2	1	1	2
S_{yh} (mm)	8.5	8	8.2	8.3	9	6.6	8.2	6.4
S_{th} (mm)	23.1	23.1	25.7	23.6	20	22.1	22.6	26
S_{tw} (mm)	10.1	8.3	9.9	15.7	8	9.4	6.9	11.1
R_{pw} (mm)	11.5	10.3	12	15.3	9	7.7	12.5	13.2
R_{ph} (mm)	8.4	7.5	7.6	10.5	10	11.6	8.8	9.7
R_{yh} (mm)	19.1	21.6	14.8	16.6	20	23.6	16.8	15.6
N_{DC}	126	126	126	126	126	126	126	126
N_{AC}	96	96	96	96	96	96	96	96
I_{DC} (A)	6.97	5.97	6.35	3.21	5.34	6.47	6.56	7.95
I_{AC} (A)	4.71	7.84	6.81	4.95	7.01	6.41	5.93	7.19

IV. PERFORMANCE COMPARISON OF OPTIMAL MODELS

Based on the optimal dimension parameters of each model, and considering two different winding designs, the comparison among the eight cases is presented in this chapter, including the magnetic field distribution, back electromotive force (EMF), average torque, torque ripple, loss and efficiency.

A. Flux distribution and back EMF

Among eight models, the layout of DC field winding keeps the same design with each DC coil across two stator teeth, hence the flux distribution of DC field is unchanged. The difference is caused by the AC armature winding design. Fig. 9 presents the flux distribution produced by armature winding in eight models. It can be seen, the flux path of proposed winding design is longer than that of the traditional counterpart regardless of the rotor pole number, because the PPN of the proposed $|3N_p\text{-}N_r|$ winding is lower than the traditional $|N_p\text{-}N_r|$ winding.

According to the flux modulation theory, the lower working harmonic order is, the higher the rotation speed is, and therefore higher back EMF and torque production can be obtained. It is worth pointing out that the 1-pole-pair armature field in the 12/10/1 and 12/8/1 cases is much easier to be saturated due to longer magnetic circuit, compared to that of the 2-pole-pair armature field in the 12/11/2 and 12/7/2 cases, which will limit the electromagnetic torque generation to some extent.
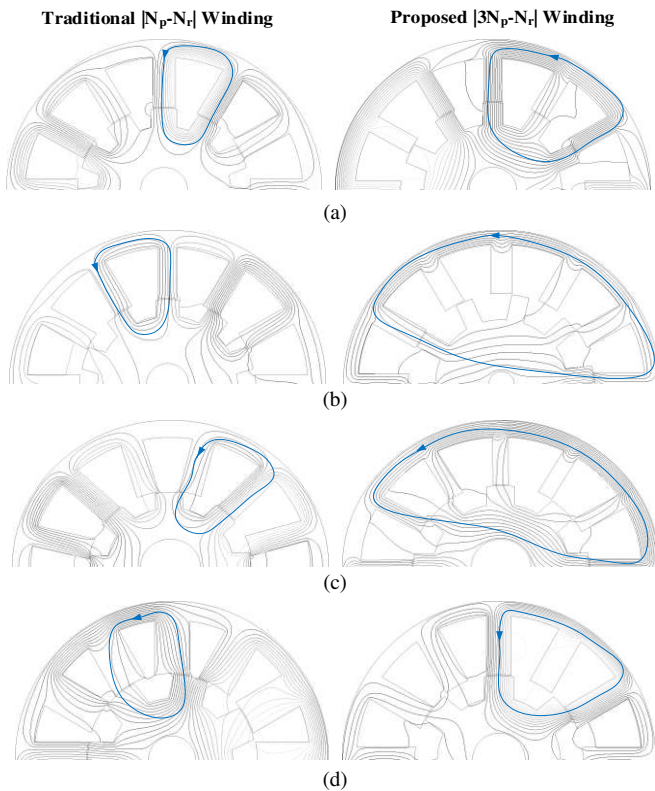
Fig. 9. Flux distribution of two different winding designs with (a) 11 rotor poles. (b) 10 rotor poles. (c) 8 rotor poles. (d) 7 rotor poles.
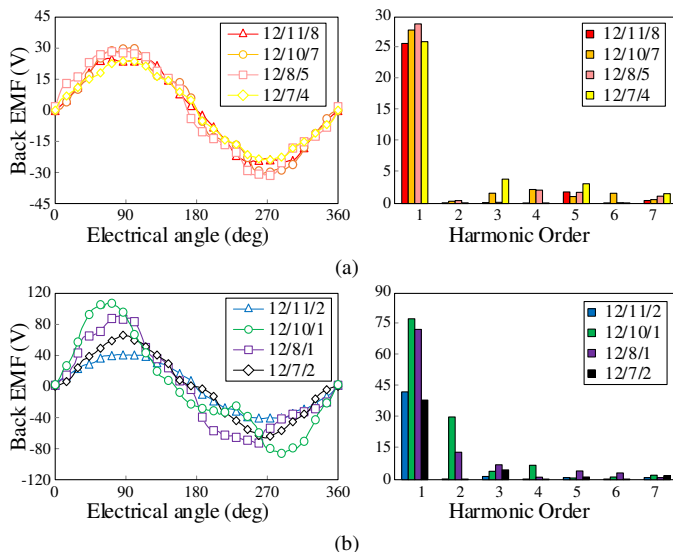

Fig. 10. Back EMF and harmonics distribution (a) Models with the traditional $|N_p\text{-}N_r|$ winding. (b) Models with the proposed $|3N_p\text{-}N_r|$ winding.

The back EMF waveforms within an electrical period at rotating speed of 900 rpm are calculated and presented in Fig. 10, along with their harmonic distribution obtained by Fast Fourier Analysis. Using the symbol of ($N_{slot}/N_r/PPN_a$) to represent each design, four models of 12/11/8, 12/10/7, 12/8/5, 12/7/4 are those having the traditional $|N_p\text{-}N_r|$ winding, while the models of 12/11/2, 12/10/1, 12/8/1, 12/7/2 employ the proposed $|3N_p\text{-}N_r|$ winding. The amplitude of back EMF of 12/11/8, 12/10/7, 12/8/5, 12/7/4 models are 25.8V, 27.9V, 28.9V, 26.0V, respectively. For 12/11/2, 12/10/1, 12/8/1, 12/7/2 models, they are 42.4V, 77.7V, 72.6V, 38.5V, respectively. This

proves the effectiveness of the proposed winding, as it contributes much higher back EMF in all cases.

The total harmonic distortion (THD) of back EMF for 12/11/8, 12/10/7, 12/8/5, 12/7/4 models are calculated as 7.5%, 13.0%, 11.6%, 20.4%, respectively, while those for 12/11/2, 12/10/1, 12/8/1, 12/7/2 models are 5.7%, 40.6%, 23.0% and 13.9%, respectively. Moreover, it can be noticed that the THDs of 12/10 and 12/8 cases are relatively higher than 12/11 and 12/7 cases, because there is no even harmonics when rotor salient pole is an odd number. Overall, 12/11/2 model can achieve the enhanced back EMF and minimum THD at the same time.

B. Torque performance

TABLE IX
TORQUE PERFORMANCE

	N_{slot}	N_r	PPN_a	Average torque	Ripple
Traditional $\|N_p - N_r\|$ winding	12	11	8	2.45 Nm	19.8%
	12	10	7	4.19 Nm	69.2%
	12	8	5	3.96 Nm	38.4%
	12	7	4	2.24 Nm	33.2%
Proposed $\|3N_p - N_r\|$ winding	12	11	2	4.30 Nm	16.7%
	12	10	1	4.03 Nm	80.8%
	12	8	1	3.01 Nm	72.0%
	12	7	2	3.36 Nm	8.9%

The torque performance of eight models is evaluated and the results are listed in Table IX, including the average torque and torque ripple ratio, under the rated current density of 6A/mm². When considering the torque ripple less than 20% as a necessary condition for industry applications, designs with odd rotor pole pair are recommended. Further, the 12/11/2 case using the proposed winding design method, shows the highest average torque among all the candidates, benefiting from higher MMF utilization of DC field harmonics.

C. Loss, efficiency, and power factor

The core loss and efficiency of the eight models are presented in Fig. 11 and Fig. 12, respectively. The DC field current and AC armature current are fixed as the rated value, with the speed varying from 0 to 1000 rpm. It can be seen, using the proposed $|3N_p\text{-}N_r|$ winding design method, the core loss is relatively higher because of the long magnetic circuit of armature winding that makes the stator core is more saturated than the traditional models. Meanwhile, since the distributed configuration is used, the copper loss of proposed winding is also higher in this case due to the increased length of winding end. Hence, the designs using the traditional winding show relatively higher efficiency. However, the influence of end copper loss can be reduced if the machine is designed with a larger ratio of length and diameter, which is more suitable for the proposed design method.

TABLE X
COPPER LOSS UNDER RATED CURRENT

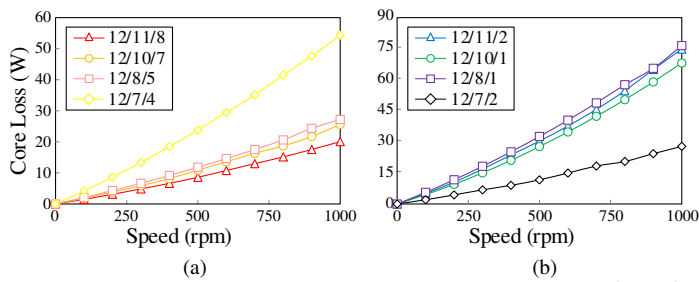|	Traditional $\|N_p\text{-}N_r\|$ winding				Proposed $\|3N_p\text{-}N_r\|$ winding			
N_{slot}	12	12	12	12	12	12	12	12
N_r	11	10	8	7	11	10	8	7
PPN_a	8	7	5	4	2	1	1	2
P_{Cu}(W)	97.89	114.03	108.92	110.21	142.98	201.92	231.7	97.51

Fig. 11.   Core loss under rated current. (a) VRMs with traditional $|N_p\text{-}N_r|$ winding. (b) VRMs with proposed $|3N_p\text{-}N_r|$ winding.
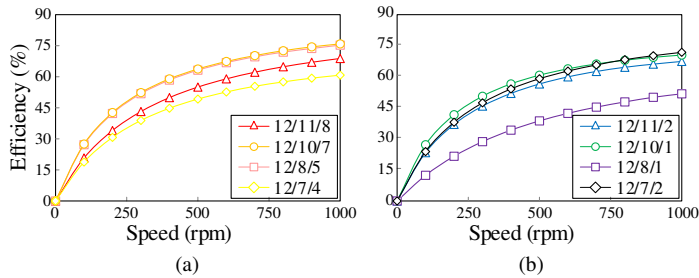

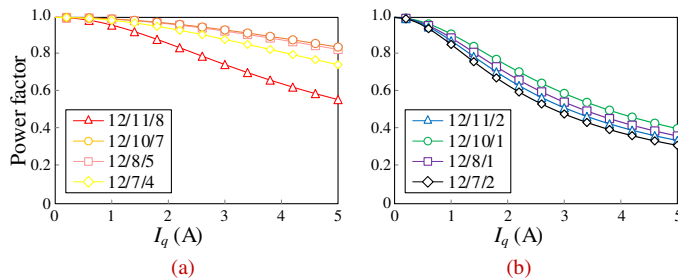Fig. 12.   Efficiency under rated current. (a) VRMs with traditional $|N_p\text{-}N_r|$ winding. (b) VRMs with proposed $|3N_p\text{-}N_r|$ winding.

Fig. 13.   Power factor under different current. (a) VRMs with traditional $|N_p\text{-}N_r|$ winding. (b) VRMs with proposed $|3N_p\text{-}N_r|$ winding.

The power factor under different current of the eight models are presented in Fig. 13. It is admitted that the proposed winding design leads to relatively lower power factor than the traditional counterpart. The reason is that proposed winding designs have lower PPN than the traditional designs, therefore, distributed winding configuration is used for proposed designs, while concentrated winding configuration is used for the traditional design. Consequently, the inductance of the proposed winding design is higher, which causes stronger armature reaction and associated lower power factor.

D. Radial magnetic force

The radial magnetic force is one important factor to affect the mechanical vibration and noise in electrical machines, which should be evaluated in the proposed design as well. Fig. 14 and Fig. 15 shows the calculated radial magnetic force between the stator and rotor under no-load and load conditions, respectively.

It is validated that there is little radial magnetic force when even rotor salient pole number is adopted under both load and no-load conditions. While for 12/11/2 with proposed new AC winding, its unbalanced radial magnetic force is non-neglectable, and it is much higher under load condition than that of no-load condition. This issue should be considered during design stage. One potential solution is to use 24/22/4 design by doubling the 12/11/2 case as the unit machine design.
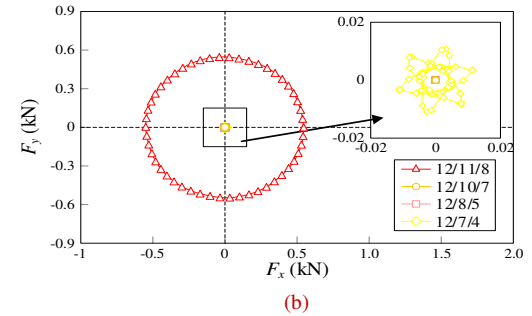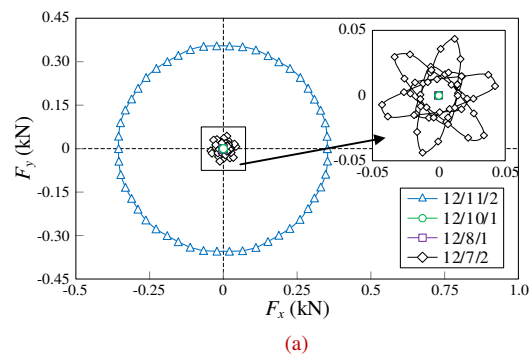

Fig. 14. Radial magnetic force under no-load condition. (a) Traditional $|N_p\text{-}N_r|$ winding design. (b) Proposed $|3N_p\text{-}N_r|$ winding design.
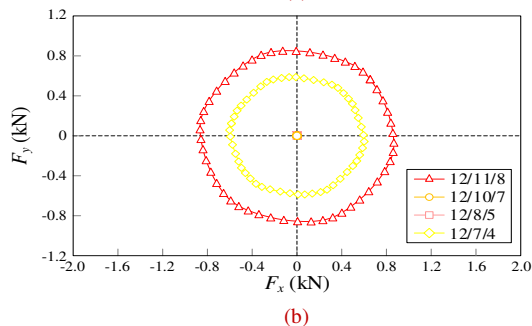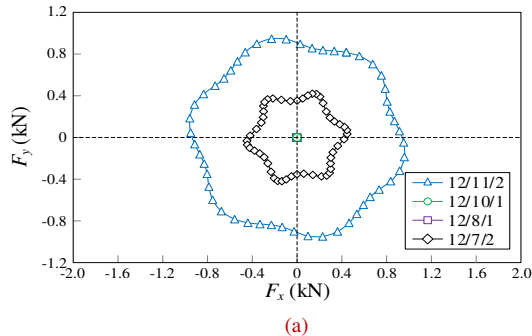
Fig. 15. Radial magnetic force under load condition. (a) Traditional $|N_p\text{-}N_r|$ winding design. (b) Proposed $|3N_p\text{-}N_r|$ winding design.

V. EXPERIMENTAL VALIDATION

In this part, a prototype of 12/11/2 design was manufactured and tested to validate the above finite element analysis. The parameters of prototype are in line with those data in Table VIII. Fig. 16 presents the manufacturing details of machine prototype and the setup of test bench, which mainly includes the magnetic powder brake, prototype, inverter, drive controller, DC power source and oscilloscope. In the testing process, the magnetic powder brake functions as a controllable load. The DC field current is provided by an independent DC power source. The

traditional vector control method of AC synchronous machine can be directly applied to the proposed machine. Using the slot/pole/winding combination of 12/11/2 case in this prototype, the winding inductance has little vibration with rotor position change. Therefore, this machine can be regarded as a non-salient machine, and the traditional $I_d=0$ vector control can be used. The control block diagram is presented in Fig. 17.

(a)   (b)   (c)

(d)

Fig. 16. The prototype and test bench setup. (a) Rotor core lamination (b) Stator core lamination. (c) Winding layout. (d) Test bench setup.
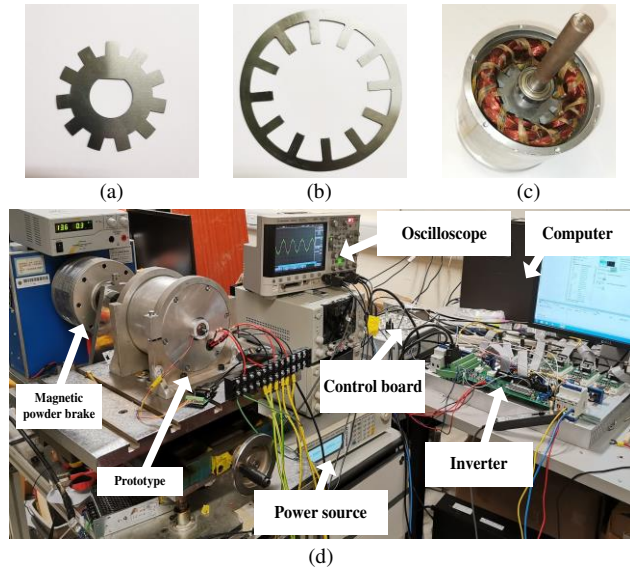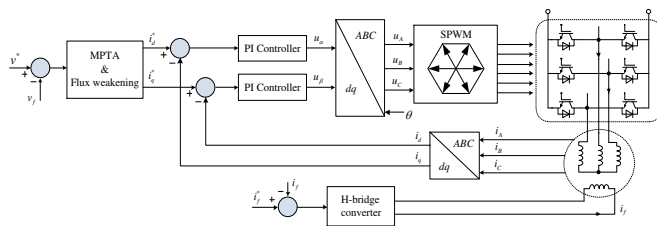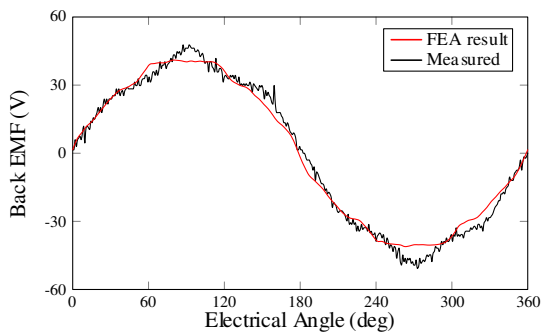

Fig. 17. Control block diagram for the prototype.

Fig. 18. Open-circuit back EMF at 900 rpm.

The open-circuit back EMF is tested at 900rpm and presented in Fig. 18. The tested result basically agrees with that of finite element analysis, while a certain distortion is observed that can be produced by mechanical fabrication tolerance. By injecting a constant DC current into armature winding and then collecting static torque at different rotor positions, the torque vs current angle curve under rated current is presented in Fig. 19, along with the FEA result. The prototype uses a salient rotor structure,

but the reluctance torque makes little contribution to the overall torque production, due to the electromagnetic complementary feature of the 12/11/2 deign. Hence, maximum torque can be obtained when current angle is near 90 deg.
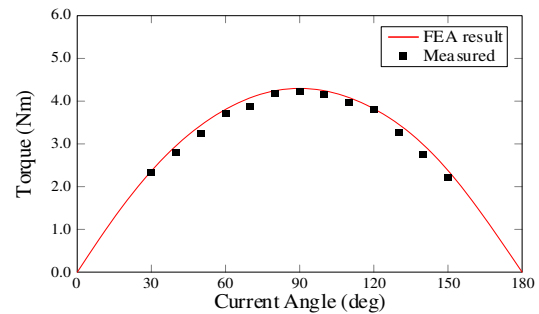
Fig. 19. Torque vs current angle curve at rated condition.
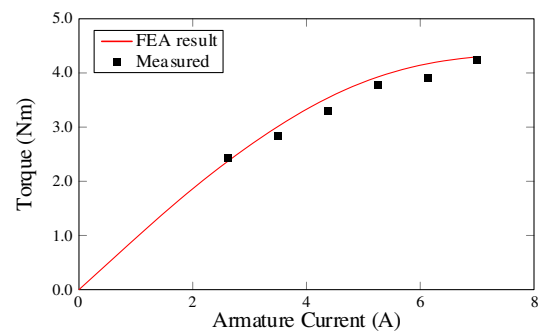
Fig. 20. Torque vs current curve, with variable AC current.
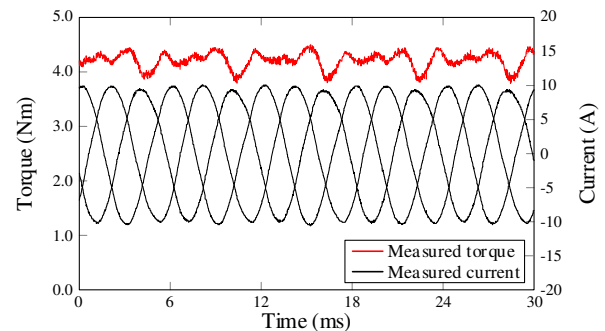
Fig. 21. Measured three-phase armature current and torque.

Further, the torque vs current curve is presented in Fig. 20, where AC current changes from zero to the rated value, while DC current keeps at the rated value all the time. Again, good agreement is achieved between testing results and FEA results. Finally, the dynamic performance is tested and given in Fig. 21. The three-phase current is measure by current sensors, while the electromagnetic torque is obtained from magnetic powder brake. The measured torque is slightly lower than the FEA predication, but it is acceptable in consideration of the error in measurement as well as mechanical fabrication tolerance.

VI. CONCLUSION

This paper proposes a novel high-order-harmonic armature winding design method for Vernier reluctance machine having DC field coils across two stator teeth, which can improve torque density by 75.6% when using 12/11 slot pole combination with

the minimum cogging torque and torque ripple.In this paper, through analyzing the flux modulation effect of DC field source, it is revealed that the flux density ratio of fundamental harmonic and third-order harmonic is about 1.24, regardless of the rotor pole pair number. Because of the rich content of third-order DC field harmonic, it is feasible to select its modulated components as the main working harmonic. Based on this, a novel winding design principle of $PPN_a=|3N_p-N_r|$ is proposed for VRMs with DC coils across two stator teeth, and further evaluated against the existing design principle of $PPN_a=|N_p-N_r|$. Finite element design and optimization are performed for four slot pole designs using two different winding configurations. Eight optimal cases are selected for performance analysis, and the results show that proposed winding design method can improve torque density significantly, while increasing the core loss and copper loss at the same time due to long magnetic circuit in yoke part and increased winding ends. Hence, the efficiency becomes slightly lower when using the proposed winding design method. Future research will focus on the improvement of machine efficiency, for instance, using a drum winding to reduce end copper loss.

REFERENCES

[1] I. Boldea, L. N. Tutelea, L. Parsa and D. Dorrell, "Automotive electric propulsion systems with reduced or no permanent magnets: an overview," *IEEE Trans. Ind. Electron.*, vol. 61, no. 10, pp. 5696-5711, Oct. 2014

[2] Y. Jung, M. Park, K. Kim, J. Chin, J. Hong and M. Lim, "Design of high-speed multilayer IPMSM using ferrite PM for EV traction considering mechanical and electrical characteristics," *IEEE Trans. Ind. Appl.*, vol. 57, no. 1, pp. 327-339, Jan. 2021

[3] Z. S. Du and T. A. Lipo, "Design of an improved dual-stator ferrite magnet Vernier machine to replace an industrial rare-earth IPM machine," *IEEE Trans. Energy Convers.*, vol. 34, no. 4, pp. 2062-2069, Dec. 2019

[4] X. Zhao, S. Niu and W. Fu, "A new modular relieving-DC-saturation Vernier reluctance machine excited by zero-Sequence current for electric vehicle," *IEEE Trans. Magn.*, vol. 55, no. 7, pp. 1-5, July 2019.

[5] N. Bianchi, S. Bolognani, D. Bon and M. Dai Pre, "Rotor flux-barrier design for torque ripple reduction in synchronous reluctance and PM-assisted synchronous reluctance motors," *IEEE Trans. Ind. Appl.*, vol. 45, no. 3, pp. 921-928, May 2009

[6] H. Cai, B. Guan and L. Xu, "Low-cost ferrite PM-assisted synchronous reluctance machine for electric vehicles," *IEEE Trans. Ind. Electron.,* vol. 61, no. 10, pp. 5741-5748, Oct. 2014

[7] K. Kiyota, T. Kakishima and A. Chiba, "Comparison of test result and design stage prediction of switched reluctance motor competitive with 60-kW rare-earth PM motor," *IEEE Trans. Ind. Electron.*, vol. 61, no. 10, pp. 5712-5721, Oct. 2014

[8] X. D. Xue, K. W. E. Cheng, and T. W. Ng, "Multi-objective optimization design of in-wheel switched reluctance motors in electric vehicles," *IEEE Trans. Ind. Electron.*, vol. 57, no. 9, pp. 2980-2987, Sep. 2010

[9] S. Mir, M. E. Elbuluk and I. Husain, "Torque-ripple minimization in switched reluctance motors using adaptive fuzzy control," *IEEE Trans. Ind. Appl.,* vol. 35, no. 2, pp. 461-468, Mar. 1999

[10] Y. Jin, B. Bilgin, and A. Emadi, "An extended-speed low-ripple torque control of switched reluctance motor drives," *IEEE Trans. Power Electron.*, vol. 30, pp. 1457-1470, Sep. 2015

[11] R. Martin, J. D. Widmer, B. C. Mecrow, A. Mebarki and N. L. Brown, "Electromagnetic considerations for a six-phase switched reluctance motor driven by a three-phase inverter," *IEEE Trans. Ind. Appl.,* vol. 52, no. 5, pp. 3783-3791, Sep. 2016

[12] Y. Wang, Z. Zhang, and Y. Yan, "Torque density improvement of doubly salient electromagnetic machine with asymmetric current control," *IEEE Trans. Ind. Electron.*, vol. 63, no. 12, pp. 7434-7443, Dec. 2016

[13] L. Shi and B. Zhou, "Analysis of a new five-phase fault-tolerant doubly salient brushless DC generator," *IET Power Electron.*, vol. 10, no. 7, pp. 633-640, Aug. 2016.

[14] C. H. T. Lee, K. T. Chau, C. Liu, T. W. Ching and F. Li, "Mechanical offset for torque ripple reduction in magnetless double-stator doubly salient machine," *IEEE Trans. Magn.*, vol. 50, no. 11, pp. 1-4, Nov. 2014

[15] Z. Chen, H. Wang and Y. Yan, "A doubly salient starter/generator with two-section twisted-rotor structure for potential future aerospace application," *IEEE Trans. Ind. Electron.*, vol. 59, no. 9, pp. 3588-3595, Sep. 2012

[16] X. Liu and Z. Q. Zhu, "Stator rotor pole combinations and winding configurations of variable flux reluctance machines," *IEEE Trans. Ind. Appl*, vol. 50, no. 6, pp. 3675-3684, Nov.-Dec. 2014.

[17] X. Zhao and S. Niu. "Design and optimization of a novel slot-PM-assisted variable flux reluctance generator for hybrid electric vehicles," *IEEE Trans. Energy Convers.*, vol. 33, no. 4, pp. 102-111, Dec. 2018.

[18] X. Liu and Z. Q. Zhu, "Comparative study of novel variable flux reluctance machines with doubly fed doubly salient machines," *IEEE Trans. Magn.*, vol. 49, no. 7, pp. 3838-3841, July 2013.

[19] S. Jia, R. Qu, J. Li, D. Li and H. Lu, "Design considerations of stator DC-winding excited Vernier reluctance machines based on the magnetic gear effect," *IEEE Trans. Ind. Appl.*, vol. 53, no. 2, pp. 1028-1037, Apr. 2017

[20] S. Jia, R. Qu, W. Kong, D. Li, J. Li, "Stator/rotor slot and winding pole pair combinations of DC-biased current Vernier reluctance machines," *IEEE Trans. Ind. Appl.*, vol. 54, no. 6, pp. 5967-5977, Dec. 2018

[21] Z. Q. Zhu, B. Lee and X. Liu, "Integrated field and armature current control strategy for variable flux reluctance machine using open winding," *IEEE Trans. Ind. Appl.*, vol. 52, no. 2, pp. 1519-1529, Mar. 2016

[22] Z. Q. Zhu and B. Lee, "Integrated field and armature current control for dual three-phase variable flux reluctance machine drives," *IEEE Trans. Energy Convers.*, vol. 32, no. 2, pp. 447-457, Jun. 2017

[23] X. Zhao and S. Niu, "A new slot-PM Vernier reluctance machine with enhanced zero-sequence current excitation for electric vehicle propulsion," *IEEE Trans. Ind. Electron.*, vol. 67, no. 5, pp. 3528-3539, May 2020

[24] Y. Du, C. Zhang, X. Zhu, et al., "Principle and analysis of doubly salient PM motor with π-shaped stator iron core segments", *IEEE Trans. Ind. Electron.*, vol. 66, no. 3, pp. 1962-1972, Mar. 2019.

[25] T. Sheng and S. Niu, "A Novel zero-sequence-current-based dual-stator biased-flux machine," *IEEE Trans. Energy Convers.*, vol. 33, no. 4, pp. 1934-1942, Dec. 2018.

[26] T. Sheng, S. Niu, W. N. Fu and Q. Lin, "Topology exploration and torque component analysis of double stator biased flux machines based on magnetic field modulation mechanism," *IEEE Trans. Energy Convers.*, vol. 33, no. 2, pp. 584-593, Jun. 2018.

[27] H. Wen, M. Cheng, Y. Jiang, M. Tong and W. Wang, "Analysis of airgap field modulation principle of flux guides," *IEEE Trans. Ind. Appl.*, vol. 56, no. 5, pp. 4758-4768, Oct. 2020.

Manuscript Title: A Novel High-Order-Harmonic Winding Design Method for Vernier Reluctance Machine with DC Coils across Two Stator Teeth

ID: 21-TIE-1062.R1

Paper Type: Regular paper

Response to Associate Editor

Four independent experts have evaluated the paper. In general, the reviewers think that the explanations and the results provided are far from sufficient to demonstrate the superiority of the proposed design method advocated in this paper. It is a major concern that the remarkable increase in torque density is perceived as quite limited (according to Reviewer 4) and lacks context to a realistic base case (opinion of Reviewer 3). In particular, the paper did neither address the inherently low torque density as a drawback of existing VRM designs. As a result, one of the main contributions of the manuscript is not justified. Moreover, Reviewer 2 thinks that the paper is not transparent enough regarding the other drawbacks as well (e.g., a low power factor). Finally, the authors are highly encouraged to revise the paper according to each of the issues raised by the reviewers. Please highlight all changes in color and clarify the changes in a separate response letter. Then the paper can be reevaluated by the same reviewers.

Our response:

We thank the Editors and Reviewers for their time and efforts in reviewing our manuscript. We have addressed the remained comments from reviewers and made all necessary changes into the revised version. The changes in the revised manuscript are typeset in "red" color.

Reply to Reviewer 1:

1. **Reviewer's comment:**

VFM at the right column of 44 line in page 1, VFM??

Response-1:

Thanks for pointing it out, we are sorry for this typo, it should be VRM (Vernier Reluctance Machine)

Changes Made:

We update the manuscript by correcting this typo. (See paragraph 4 of Introduction).

2. **Reviewer's comment:**

Figure 3, are you sure the MMF is for two stator teeth of presented winding design?

Response-2:

Thanks for pulling up this question. Fig. 3 in the manuscript is for the MMF waveform of DC field coils across two stator teeth, rather than the proposed armature winding design. As is presented below, when only DC current excitation is applied, the amplitude of MMF under every stator tooth is the same due to magnetic symmetry, and the polarity of MMF is changed every two teeth.
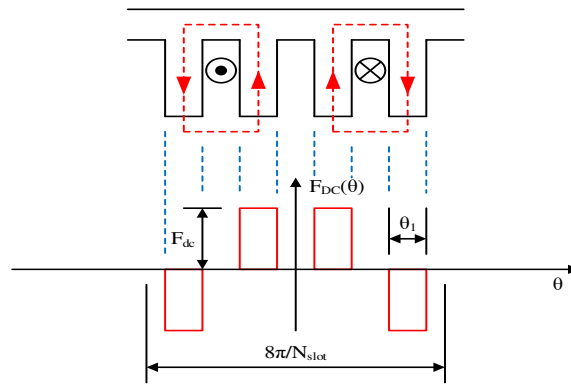
Fig. 3. MMF waveform of DC current.

Changes Made:

We have updated the manuscript by adding more discussion about the MMF waveform generated by DC field current. (See the illustration of Fig. 3 in Part B of Section II)

3. **Reviewer's comment:**

Not clearly define mechanical and electrical angle / rotating speed in tables and figures.

Response-3:

Thanks for your comment.The mechanical angle (θ_{me}) is defined as the angular difference between the measured rotor position and the initial rotor position. The electrical angle (θ_{el}) is defined as:

$$\theta_{el} = N_r \theta_{me}$$

where N_r is the number of rotor salient poles. It can be seen, the electrical angle (θ_{el}) is in direct proportion to the mechanical angle (θ_{me}).

Further, the mechanical speed (ω_{me}) and electrical speed (ω_{el}) can be defined as:

$$\omega_{me} = \frac{d}{dt}\theta_{me}$$

$$\omega_{el} = \frac{d}{dt}\theta_{el}$$

Similarly, the electrical speed (ω_{el}) is in direct proportion to the mechanical speed (ω_{me}).

In general, in the design and analysis of electrical machines, the mechanical angle is usually used when analyzing space-related performance including air gap field MMF, permeance distribution, flux density distribution, etc. The electrical angle is usually used for time-related performance including back EMF, torque production, current angle, etc.

Changes Made:

We have updated the manuscript by adding the definition of mechanical angle and electrical angle in the corresponding illustrations of machine performance. (See the illustration of Fig. 3, in Part B of Section II and Fig. 10, in Part A of Section IV)

4. **Reviewer's comment:**

Table 10 and table IV, does not match each other (12/11 case),

Response-4:

Thanks for your advice. As there is no Table 10 in the original manuscript, we believe that you refer to Fig. 6 and Table IV (12/11 case). We are sorry for this mistake in Fig. 6(a) as the main working harmonics are marked by mistake in the 12/11 case. We have corrected the mistake, and the data of Fig. 6 are now in line with Table IV in the updated manuscript.

Changes Made:

We update the manuscript by correcting the mistake in Fig. 6(a) (See Part D of Section II).

5. **Reviewer's comment:**

In Fig. 8, the showed torque ripple is much larger than that presented in table V, why? is Torque in x-axis average?

Response-5:

Thanks for pointing out this concern. The results in Fig. 8 are the Pareto front of the Genetic Algorithm optimization in the last generation. Each point represents a model, and the x-axis and y-axis coordinate represent the average torque value and torque ripple, respectively. For each slot/pole/winding design, only one optimal model is selected from the corresponding Pareto front, considering the tradeoff between average torque value and torque ripple. And their corresponding torque performance index are listed in Table IX below.

TABLE IX

TORQUE PERFORMANCE OF OPTIMAL DESIGNS

	N_{slot}	N_r	PPN_a	Average torque	Ripple
Traditional $\lvert N_p - N_r \rvert$ winding	12	11	8	2.45 Nm	19.8%
	12	10	7	4.19 Nm	69.2%
	12	8	5	3.96 Nm	38.4%
	12	7	4	2.24 Nm	33.2%
Proposed $\lvert 3N_p - N_r \rvert$ winding	12	11	2	4.30 Nm	16.7%
	12	10	1	4.03 Nm	80.8%
	12	8	1	3.01 Nm	72.0%
	12	7	2	3.36 Nm	8.9%

Fig. 8. Optimization results of the last generation (Pareto front). (a) Traditional $\lvert N_p\text{-}N_r \rvert$ winding design. (b) Proposed $\lvert 3N_p\text{-}N_r \rvert$ winding design.

Changes Made:

We update the manuscript by marking the optimal designs in the Pareto front of Fig. 8. Besides, the label of x-axis coordinate has been changed from "Torque" to "Average torque value", which is more clear for readers to understand. (See Fig. 8 and related illustration, in Section III).

6. **Reviewer's comment:**

"sdis" at the right column of 44 line at page 5, Mis-printing?

Response-6:

Thanks for pointing it out. We are sorry for this typo, the correct word should be "is".

Changes Made:

We have updated the manuscript by correcting the typo. (See Part A of Section IV).

7. **Reviewer's comment:**

More analysis should be given to figure 9, why the flux distribution is good / bad for producing torque in the presented winding design.

Response-7:

Thanks for your advice. The flux distribution in Fig. 9 is to validate the pole pair number (PPN) of the main working harmonic produced by two different winding designs. Because the PPN of the proposed $\left|3N_p - N_r\right|$ winding is relatively lower, the magnetic path of the proposed winding is longer than that of traditional counterpart, which agrees with the results in Fig. 9. According to the flux modulation theory, the rotation speed of working harmonic is in inverse proportion to harmonic order. The lower order of working harmonic is, the higher rotation speed can be achieved, and thus higher back EMF and torque production can be obtained. This is the motivation of the proposed novel high-order-harmonic winding design method to improve torque density. The quantitative analysis of harmonics contribution on back EMF and torque production can be referred in Response-11 as requested by Reviewer 2 as well, which has been also added in Part E of Section II in the revised manuscript.

Changes Made:

We have updated the manuscript by adding more analysis about the Fig. 9 (See Part A of Section IV). The quantitative analysis of the proposed winding design in enhanced back EMF and torque generation has been added as well. (See Part E of Section II.)

Reply to Reviewer 2:

1. **Reviewer's comment:**

Please explain clearly the reasons of low torque density drawback of existing VRM structures and report the values.

Response-8:

Thanks for pulling up this question. The reasons for low torque density of existing VRM structures include: (1) The flux linkage in each armature coil is biased, thus the stator core utilization factor is relatively low. (2) Some working harmonics in the air gap are not fully utilized when using the traditional winding design method. Therefore, in this manuscript, we propose a new winding

design method to better utilize the high-order airgap harmonics to boost torque density. As for the torque density value, we provide data from references [17-18], that is within 5.1 to 5.6 kNm/m^3

[17] Qu, J. Li, D. Li and H. Lu, "Design considerations of stator DC-winding excited Vernier reluctance machines based on magnetic gear effect," IEEE Trans. Ind. Appl., vol. 53, no. 2, pp. 1028-1037, Apr. 2017.

[18] X. Liu and Z. Q. Zhu, "Comparative study of novel variable flux reluctance machines with doubly fed doubly salient machines," IEEE Trans. Magn., vol. 49, no. 7, pp. 3838-3841, July 2013.

Changes Made:

We have updated the manuscript by adding more related discussions about the torque density of existing VRM structures (See introduction part).

2. **Reviewer's comment:**

Another disadvantage of Vernier type machines is low power factor. This is not discussed and addressed for traditional and proposed winding design methods in your study.

Response-9:

Thanks for your suggestion. The power factors of 8 optimal models with different winding designs are calculated and listed as follows.
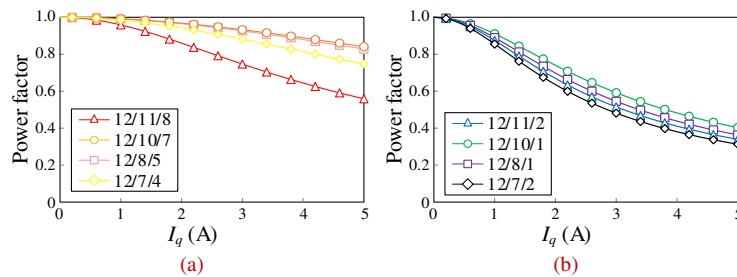
Fig. 13.   Power factor vs load current. (a) Traditional $\left|N_p\text{-}N_r\right|$ winding design. (b) Proposed $\left|3N_p\text{-}N_r\right|$ winding design.

It is admitted that the proposed winding design leads to relatively lower power factor than the traditional counterpart, the reason is that proposed winding designs have lower PPN than the traditional designs, therefore, distributed winding configuration is used for proposed designs, while concentrated winding configuration is used for the traditional counterparts. Consequently, the inductance of the proposed winding design is higher, which causes stronger armature reaction and associated lower power factor, according to the following power factor equation.

$$PF = \frac{\varphi_f}{\sqrt{\varphi_f^2 + \left(L_q I_q\right)^2}}$$

where φ_f is the main flux linkage and I_q is the q-axis current.

Changes Made:

We have updated the manuscript by adding the analysis on power factor in Part C of Section IV.

3. **Reviewer's comment:**

The winding layouts of the proposed DC field winding across two stator teeth and traditional winding should be added to the text with discussion on the rules for creating the same MMFs (a fair comparison) considering fabricating limitations.

Response-10:

Thanks for your comments. In this manuscript, the proposed winding design method is for the AC armature winding, rather than DC field winding. Compared with the traditional DC field windings which are fully wound on every stator tooth, the DC field windings of the proposed machine are uniformly distributed across every two stator teeth. The 3D layouts of two types of DC filed winding are presented below. In terms of fabricating limitations, there is little manufacturing difficulty for two types of DC field windings. The main difference is, using DC field coils across two stator teeth can reduce the coil number by half, while the total coil ends are almost unchanged compared to the traditional design with DC coils fully wound on every tooth.
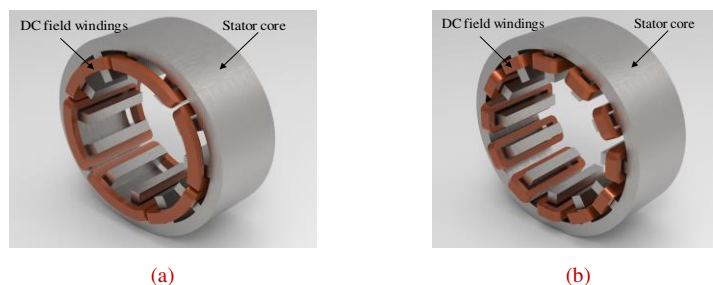
Fig. 22.   Winding layout of two types of DC field windings. (a) Across two stator teeth. (b) Wound on every stator tooth.

The analysis on airgap MMF from two DC field windings is presented as follow. For a fair comparison, the amplitude of MMF is assumed to be the same, and the waveforms of them are presented as follow.
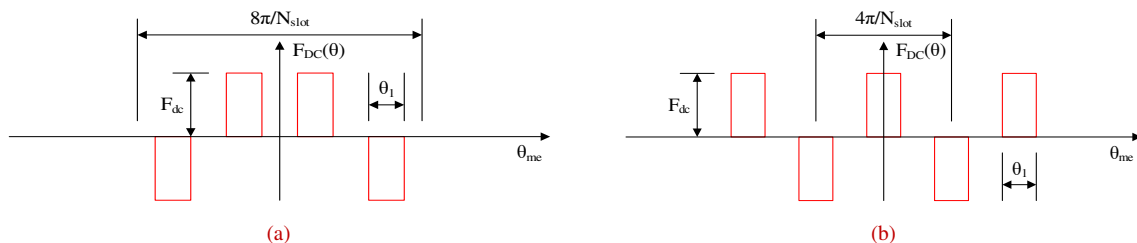
Fig. 23.   MMF of two different layouts of DC field windings. (a) Across two stator teeth. (b) Wound on every stator tooth.

The MMF of DC field windings across two stator teeth can be deduced in detail as follow:

$$F_{DC}(\theta) = \sum_{n=1}^{+\infty} F_n \cos\left(n\frac{N_{slot}}{4}\theta\right)$$

$$F_n = \frac{N_{slot}}{4\pi} \int_{-\frac{4\pi}{N_{slot}}}^{\frac{4\pi}{N_{slot}}} F_{DC}(\theta)\cos\left(n\frac{N_{slot}}{4}\theta\right)d\theta$$

$$= \frac{N_{slot}}{2\pi}\left[\int_{\frac{\pi}{N_{slot}}-\frac{\theta_1}{2}}^{\frac{\pi}{N_{slot}}+\frac{\theta_1}{2}} F_{dc}\cos\left(n\frac{N_{slot}}{4}\theta\right)d\theta - \int_{\frac{3\pi}{N_{slot}}-\frac{\theta_1}{2}}^{\frac{3\pi}{N_{slot}}+\frac{\theta_1}{2}} F_{dc}\cos\left(n\frac{N_{slot}}{4}\theta\right)d\theta\right]$$

$$= \frac{N_{slot}}{2\pi}\left[\frac{4F_{dc}}{N_{slot}n}\sin\left(n\frac{N_{slot}}{4}\theta\right)\Big|_{\frac{\pi}{N_{slot}}-\frac{\theta_1}{2}}^{\frac{\pi}{N_{slot}}+\frac{\theta_1}{2}} - \frac{4F_{dc}}{N_{slot}n}\sin\left(n\frac{N_{slot}}{4}\theta\right)\Big|_{\frac{3\pi}{N_{slot}}-\frac{\theta_1}{2}}^{\frac{3\pi}{N_{slot}}+\frac{\theta_1}{2}}\right]$$

$$= \frac{4F_{dc}}{n\pi} \sin\left(n\frac{N_{slot}}{8}\theta_1\right)\left[\cos\left(\frac{n\pi}{4}\right) - \cos\left(\frac{3n\pi}{4}\right)\right]$$

Suppose the stator tooth has the same angular size with slot open, which means $\theta_1 \approx \frac{\pi}{N_{slot}}$, , the

amplitude ratio between fundamental harmonic and 3rd harmonic can be deduced as follows.

$$\frac{|F_1|}{|F_3|} = \frac{\left|\frac{4F_{dc}}{\pi}\sin\left(\frac{N_{slot}}{8}\theta_1\right)\left[\cos\left(\frac{\pi}{4}\right) - \cos\left(\frac{3\pi}{4}\right)\right]\right|}{\left|\frac{4F_{dc}}{3\pi}\sin\left(3\frac{N_{slot}}{8}\theta_1\right)\left[\cos\left(\frac{3\pi}{4}\right) - \cos\left(\frac{9\pi}{4}\right)\right]\right|} \approx 1.24$$

Therefore, the 3rd harmonics in the MMF is abundant in this type of DC field windings, as the amplitude of fundamental harmonic is close to 3rd harmonic. For a detailed comparison, the MMF of DC field windings wound on every stator tooth is analyzed as follow.

$$F_{DC}(\theta) = \sum_{n=1}^{+\infty} F_n \cos\left(n\frac{N_{slot}}{2}\theta\right)$$

$$F_n = \frac{N_{slot}}{2\pi} \int_{-\frac{4\pi}{N_{slot}}}^{\frac{4\pi}{N_{slot}}} F_{DC}(\theta)\cos\left(n\frac{N_{slot}}{2}\theta\right)d\theta$$

$$= \frac{N_{slot}}{\pi}\left[\int_0^{\frac{\theta_1}{2}} F_{dc}\cos\left(n\frac{N_{slot}}{2}\theta\right)d\theta - \int_{\frac{2\pi}{N_{slot}}-\frac{\theta_1}{2}}^{\frac{2\pi}{N_{slot}}} F_{dc}\cos\left(n\frac{N_{slot}}{2}\theta\right)d\theta\right]$$

$$= \frac{N_{slot}}{\pi}\left[\frac{2F_{dc}}{nN_{slot}}\sin\left(n\frac{N_{slot}}{2}\theta\right)\Big|_0^{\frac{\theta_1}{2}} - \frac{2F_{dc}}{nN_{slot}}\sin\left(n\frac{N_{slot}}{2}\theta\right)\Big|_{\frac{2\pi}{N_{slot}}-\frac{\theta_1}{2}}^{\frac{2\pi}{N_{slot}}}\right]$$

$$= \frac{2F_{dc}}{n\pi}\left[\sin\left(n\frac{N_{slot}}{4}\theta_1\right) - \sin(n\pi) + \sin\left(n\pi - n\frac{N_{slot}}{4}\theta_1\right)\right]$$

Similarly, suppose the stator tooth has the same angular size with slot open, which means $\theta_1 \approx \frac{\pi}{N_{slot}}$, the amplitude ratio between fundamental harmonic and 3rd harmonic can be deduced as

$$\frac{|F_1|}{|F_3|} = \frac{\left|\frac{2F_{dc}}{\pi}\left[\sin\left(\frac{N_{slot}}{4}\theta_1\right) - \sin(\pi) + \sin\left(\pi - \frac{N_{slot}}{4}\theta_1\right)\right]\right|}{\left|\frac{2F_{dc}}{3\pi}\left[\sin\left(3\frac{N_{slot}}{4}\theta_1\right) - \sin(3\pi) + \sin\left(3\pi - 3\frac{N_{slot}}{4}\theta_1\right)\right]\right|} \approx 3$$

It is shown the amplitude of 3rd harmonic is much lower than that of fundamental harmonic when using the traditional DC field winding wound every stator tooth. Therefore, the proposed high-order-harmonic winding design method is not recommended for the traditional DC layout.

Changes Made:
We have updated the manuscript by highlighting the comparison between the MMFs of two DC filed windings (See Part C of Section II).

4. **Reviewer's comment:**

It is better to add the analytical operating principles of VRM.

Eq. 2: The reasons for selecting third harmonic order is not clear. Please discuss on the problems of traditional winding design method and the expected improvements using the new design method. Also, add analytical relation of electro-magnetic torque to show the effect of air-gap flux density components of DC field winding.

Response-11:

Thanks for your comments. The key reason for selecting third harmonic order is that the main working harmonic of proposed winding has much higher rotation speed than traditional counterpart, and thus provide higher back EMF and torque generation. The detailed analytical operating principle of VRM is provided as follow.

The electromagnetic torque production is in direct proportion to open-circuit back EMF if core saturation can be neglected. And the relationship between the air-gap flux density and the corresponding back EMF can be described as follows.

$$E_{phn} = \frac{4.44 D L T_{ph}}{60} (B_n k_{wn} \omega_n)$$

where D is the diameter of the airgap circumference, L is the stack length, T_{ph} is the number of turns in a phase, E_{phn} is the amplitude of back EMF contributed by nth harmonic, B_n is the amplitude of nth harmonic, ω_n is the rotation speed of nth harmonic and k_{wn} is the winding factor of nth harmonic, which can be expressed as

$$k_{wn} = k_{pn} k_{dn}$$

where k_{pn} is the pitch factor of nth harmonic and k_{dn} is the distribution factor of nth harmonic. The open-circuit back EMF produced by each harmonic and their amplitude, rotation speed and winding factor are listed in Table V and Table VI, using 12/11/8 and 12/11/2 as the examples. The harmonics with the order higher than 32 are neglected as contributions are too small.

Although the amplitude of each air-gap flux harmonic of the traditional 12/11/8 design and proposed 12/11/2 design are the same, the corresponding winding factors are different. The main working harmonics are 4-pole-pair and 8-pole-pair for the traditional design, while that is 2-pole-pair for the proposed one. Although the amplitude of 2-pole-pair harmonic is relatively lower, the rotation speed is much higher. Therefore, the open-circuit back EMF of the proposed winding design is higher than the traditional counterpart. The analytical ratio of back EMF between two winding designs is 1.814, which agrees with the FEA result of 1.934 (error = 6.86%). A similar analysis has been applied to other six models. And the relevant data are presented in Appendix in the end of this response letter. Overall, the analytical results agree with the FEA results for all eight models.

In general, according to the flux modulation theory, the rotation speed of modulated harmonic is in inverse proportion to harmonic order. The lower order of working harmonic order is, the higher rotation speed can be achieved, and thus the higher back EMF and torque production can be obtained. This is the motivation of the proposed novel high-order-harmonic winding design method to improve torque density.

TABLE V
OPEN-CIRCUIT BACK EMF CONTRIBUTION FROM DIFFERENT HARMONICS IN 12/11/8 MODEL

Order	(n,k)	B_n (T)	ω_n	k_{pn}	k_{dn}	k_{wn}	$B_n\omega_n k_{wn}$	$\sum B_n\omega_n k_{wn}$
2	(3,-1)	0.1093	$11\omega_{me}/2$	0.5	0	0	0	
4	(5,-1)	0.0755	$11\omega_{me}/4$	0.866	1	0.866	$0.1798\omega_{me}$	
8	(1,-1)	0.1419	$11\omega_{me}/8$	0.866	1	0.866	$0.1690\omega_{me}$	
10	(7,-1)	0.0376	$11\omega_{me}/10$	0.5	0	0	0	
14	(-1,-1)	0.1433	$11\omega_{me}/14$	-0.5	0	0	0	
16	(9,-1)	0.007	$11\omega_{me}/16$	-0.866	1	-0.866	$-0.004\omega_{me}$	$0.3072\omega_{me}$
20	(-3,-1)	0.1096	$11\omega_{me}/20$	-0.866	1	-0.866	$-0.0522\omega_{me}$	
22	(11,-1)	0.0114	$11\omega_{me}/22$	-0.5	0	0	0	
26	(-5,-1)	0.0704	$11\omega_{me}/26$	0.5	0	0	0	
28	(13,-1)	0.0198	$11\omega_{me}/28$	0.866	1	0.866	$0.0067\omega_{me}$	
32	(-7,-1)	0.0370	$11\omega_{me}/32$	0.866	1	0.866	$0.0110\omega_{me}$	

TABLE VI
OPEN-CIRCUIT BACK EMF CONTRIBUTION FROM DIFFERENT HARMONICS IN 12/11/2 MODEL

Order	(n,k)	B (T)	ω_n	k_p	k_d	k_w	$B\omega_n k_w$	$\sum B\omega_n k_w$
2	(3,-1)	0.1093	$11\omega_{me}/2$	1	1	1	$0.6010\omega_{me}$	
4	(5,-1)	0.0755	$11\omega_{me}/4$	0	0	0	0	
8	(1,-1)	0.1419	$11\omega_{me}/8$	0	0	0	0	
10	(7,-1)	0.0376	$11\omega_{me}/10$	1	1	1	$0.0413\omega_{me}$	
14	(-1,-1)	0.1433	$11\omega_{me}/14$	-1	1	-1	$-0.1125\omega_{me}$	
16	(9,-1)	0.007	$11\omega_{me}/16$	0	0	0	0	$0.5573\omega_{me}$
20	(-3,-1)	0.1096	$11\omega_{me}/20$	0	0	0	0	
22	(11,-1)	0.0114	$11\omega_{me}/22$	-1	1	-1	$-0.0057\omega_{me}$	
26	(-5,-1)	0.0704	$11\omega_{me}/26$	1	1	1	$0.0298\omega_{me}$	
28	(13,-1)	0.0198	$11\omega_{me}/28$	0	0	0	0	
32	(-7,-1)	0.0370	$11\omega_{me}/32$	0	0	0	0	

Changes Made:

We have updated the manuscript by adding the mechanism of why the harmonics modulated from 3rd harmonic is a better solution as the main working harmonic. The analytical result of 12/11/8 and 12/11/2 cases are listed in detail and updated in the revised manuscript. (See Part E of Section II). The analytical results of other six models are presented in Appendix in the Response letter and briefly introduced in the revised manuscript due to page limit.

5. **Reviewer's comment:**

Section II.B: what do you mean from the following sentence:

"provides more design feasibility in the proposed VRMs to reselect the main working harmonic and boost torque generation"

Response-12:

Thanks for your concern. In this paper, we propose a new $|3N_p - N_r|$ winding design method to reselect the high-order harmonics as the main working harmonics in VRM structures. Because the reselected main working harmonic has higher rotating speed, enhanced back EMF and torque generation can be achieved. The detail analysis of harmonics contribution on back EMF will be expanded in the Part E. Overall, the proposed winding design method breaks the traditional $|N_p - N_r|$ winding design principle based on the flux modulation theory of fundamental harmonic, and thus provides more feasible slot pole combinations and winding design choices.

Changes Made:

We have updated the manuscript by changing some related comment to this sentence so that it is easier to be understood. (See the Part C of Section II)

6. **Reviewer's comment:**

The magnitude of B(1,-1) is higher than the magnitude of B(3,-1) in the case of 12/10, 12/8 and 12/7 configurations (Figs. 16 (b), (c) and (d)). However, this is not valid in the case of 12/11 configurations (Fig. 16(a)). The reasons of differences between FE results of B(1,-1)/B(3,-1) ratios and 1.24 should be explained.

Response-13:

Thanks for your suggestion. We are sorry for this mistake in Fig. 6 as the main working harmonics are marked by mistake in 12/11 case. We have corrected the mistake and the data of Fig. 6 are in line with Table IV in the updated manuscript. Now, all the FEA results agree with the analytical calculation.

The analytical result of $B_{(1,-1)}/B_{(3,-1)}$ ratio is deduced to be 1.24 when the mechanical angle of stator tooth is assumed in close to that of the adjacent stator slot opening, which means

$$\theta_1 \approx \frac{\pi}{4N_p}$$

where θ_1 is the mechanical angle of stator tooth, and N_p is the pole pair number of DC field winding. However, in the FEA models, the mechanical angle is not exactly the same with slot opening angle. Therefore, there are differences between FE results and analytical results.

Changes Made:

We have updated the manuscript by correcting the mistake in Fig. 6(a). And a short explanation for the difference between analytical and FEA results is added. (See Part D of Section II)

7. **Reviewer's comment:**

Fig. 10: analytical relations supporting the findings (increased BEMF magnitude and harmonic distortion) are not included in the manuscript.

Response-14:

Thanks for your advice. The back EMF magnitude can be increased when proposed winding design is used because the rotation speeds of main working harmonics is higher. The detailed analysis about the contribution of each air-gap harmonic on back EMF generation have been presented in the above Reponse-11 as requested by the reviewer.

As for the total harmonic distortion (THD), it is found that the 12/11 and 12/7 cases have much lower THD than 12/10 and 12/8 cases. The reason is that the winding factors of the airgap field harmonics, which produce even harmonics in back EMF, are zero in 12/11 and 12/7 cases. Therefore, the THDs of 12/11 and 12/7 cases are much lower than those of 12/10 and 12/8 cases, due to the lack of even harmonics in back EMF.
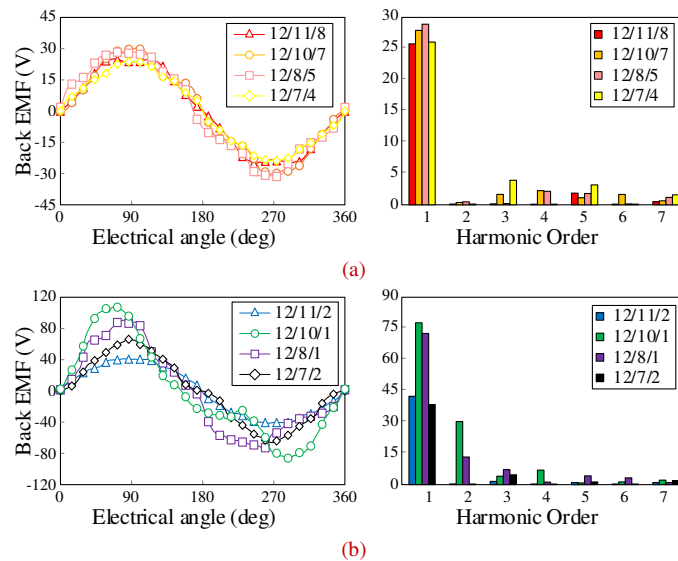
(a)

(b)

Fig. 10.   Back EMF and harmonics distribution (a) Models with the traditional $\left|N_p\text{-}N_r\right|$ winding. (b) Models with the proposed $\left|3N_p\text{-}N_r\right|$ winding.

Changes Made:

We have updated the manuscript by adding the related analysis about the amplitude of back EMF (See Part E of Section II) and the THD of back EMF (See Part A of Section IV).

8. **Reviewer's comment:**

Fig. 17: the measured torque ripple magnitude is much lower than the reported FE value in Table V.

Response-15:

Thanks for your concern. In the original manuscript, the y-label of tested torque (numbered as Fig. 17 in original manuscript, while Fig. 21 in revised manuscript) starts from -6 Nm, rather than 0 Nm, which may lead to misreading in the original manuscript. We have updated the labels of the figure to avoid misreading. The torque ripple ratio from FEA and tested results are 16.7% and 19.7%, respectively. The error in torque ripple is acceptable, considering the fabrication error and the difficulty in transient torque measurement due to the bandwidth limitation of torque senor.
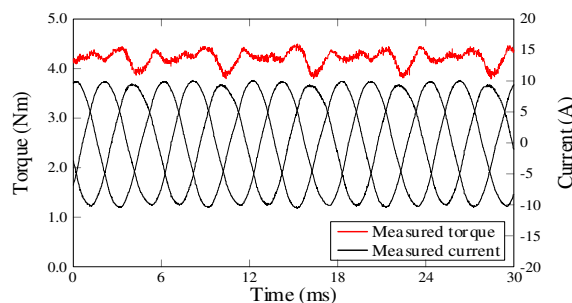
Fig. 21.   Measured three-phase armature current and torque.

Changes Made:

We have updated the manuscript by changing the labels of Fig.21 (numbered as Fig. 17 in original manuscript) to avoid misreading (See Section V).

9. **Reviewer's comment:**

Please add some details on control method used in experimental tests.

Response-16:

Thanks for your advice. The traditional vector control method of AC synchronous machine can be directly applied to the proposed machine. Using the slot/pole/winding combination of 12/11/2 case in this prototype, the winding inductance has little vibration with rotor position change. Therefore, this machine can be regarded as a non-salient machine, and the traditional I_d=0 vector control can be used. The control block diagram is presented as follows.
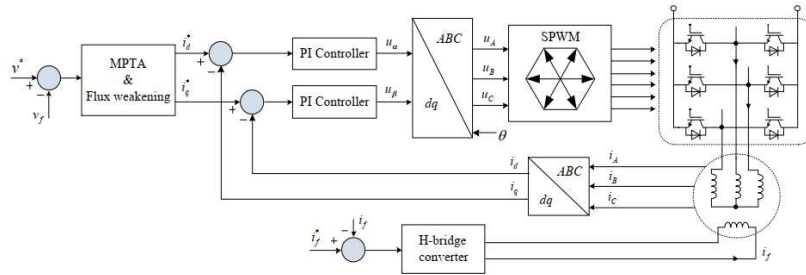
Fig. 17. Control block diagram.

Changes Made:

We have updated the manuscript by adding the Fig.17 to explain control method used in experimental tests. (See Section V)

Reply to Reviewer 3:

1. **Reviewer's comment:**

The paper is in general well written but needs language editing.

Response-17:

Thanks for pulling up this question. We have updated the manuscript with the help of experts in terms of language editing.

2. **Reviewer's comment:**

References [24]-[26] given in the introduction do not match with the two-stator-slot-pitch DC coil machine, as these references are about PM machines? The authors must confirm their statement with references that the VRM with two-stator-slot-pitch DC coils is an "emerging non-PM candidate".

Response-18:

Thanks for your suggestion. It should be admitted that references [24-26] are related to PM machines. However, the PM arrangement in these machines is the same as DC coil layout in the proposed machines, both across two stator slots. This means, the magnetomotive force distribution of both PMs and DC coils are the same, and hence the airgap harmonics order and the principle of

AC armature winding design are the same in both PM machines and DC-excited counterparts. This manuscript focuses on the investigation of DC-excited Vernier reluctance machines. Because the references of DC-excited design are not sufficient, we use the corresponding PM machine as a reasonable counterpart to support the existing literature.

3. **Reviewer's comment:**
    Also, in the introduction, the authors must explain for the reader what "symmetrical magnetic circuit" means.

    Response-19:
    Thanks for your advice. The symmetrical magnetic circuit means that each stator tooth has the same distance to the excitation source (DC field coils or PMs).
    For a clearer illustration, two machines presented below are taken as examples. For the machine in the left, there are three stator teeth designed between adjacent DC coils, the stator tooth in the middle is farther from excitation source, compared with the adjacent tooth. Therefore, the magnetic path in phase B is longer than those of phase A and C, which leads to unbalanced three-phase winding. By comparison, for the machine in the right, each stator tooth has the same distance to DC coils, and therefore, this magnetic circuit is symmetrical magnetic circuit, which helps in balanced winding and associate torque ripple.
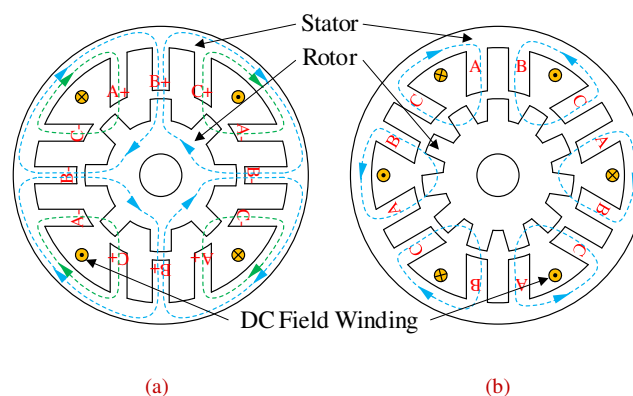
Fig. 24.   Machines for comparison. (a) Asymmetrical magnetic circuit. (b) Symmetrical magnetic circuit.

[13] L. Shi and B. Zhou, "Analysis of a new five-phase fault-tolerant doubly salient brushless DC generator," *IET Power Electron.*, vol. 10, no. 7, pp. 633-640, Aug. 2016.

Abstract: The fault-tolerant ability of a multi-phase doubly salient electromagnetic generator (DSEG) makes it suitable for important applications. However, **asymmetric phase windings** are a drawback of the traditional five-phase DSEG. This study presents the design of a new five-phase brushless DSEG **with symmetrical phases** and a robust rotor.

We hope this can clarify your concern about "symmetrical magnetic circuit". We have added this reference to support the statement. Because this is not the key point in our proposed design, we do not expand it to much considering page limit.

Changes Made:
We have updated the manuscript by adding the related reference [13]. (See introduction)

4. **Reviewer's comment:**

Together with this, the authors must state in the paper if the 12/11/2 machine of Fig. 1 and with its new AC winding, has balanced radial magnetic forces (between stator and rotor) or not along the air gap of the machine under no-load and load conditions. This is important to state this for the reader.

Response-20:

Thanks for your comment. The 12/11/2 machine in Fig.1 with its new AC winding has unbalanced radial magnetic force between stator and rotor in both no-load and load conditions. This is because the odd rotor teeth number is used, regardless of the AC winding designs. To eliminate the unbalanced radial magnetic force, we can derive out 24/22/4 counterpart by doubling the 12/11/2 case as the unit machine design.

In the revised manuscript, the radial magnetic forces of all eight models using two different winding designs are evaluated and presented as follows. It is shown there is little radial magnetic force when even rotor teeth number is adopted under both load and no-load conditions. While for 12/11/2 with proposed new AC winding, its unbalanced radial magnetic force is non-neglectable, and it is relatively higher under load condition than that of no-load condition. This issue should be considered during design stage. One potential solution is to use 24/22/4 counterpart by doubling the 12/11/2 case as the unit machine design.
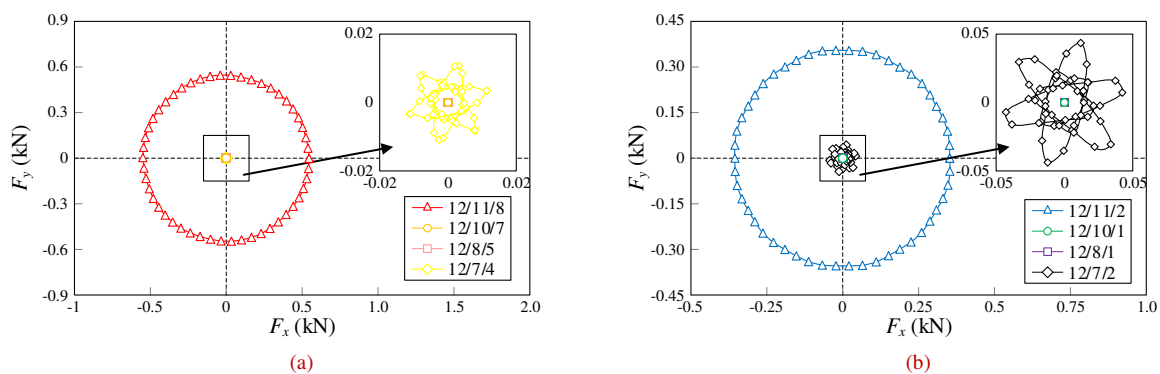
Fig. 14.   Radial magnetic force under no-load condition. (a) Traditional $\left| N_p - N_r \right|$ winding design. (b) Proposed $\left| 3N_p - N_r \right|$ winding design.
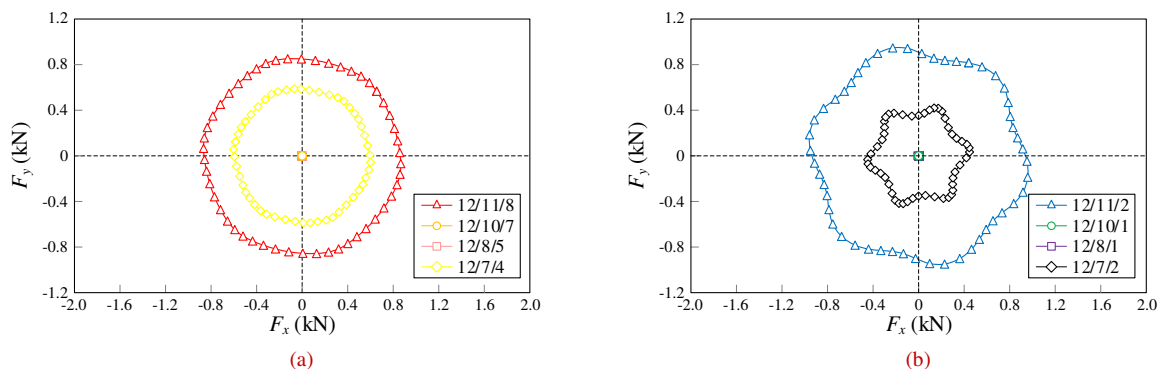
Fig. 15.   Radial magnetic force under load condition. (a) Traditional $\left| N_p - N_r \right|$ winding design. (b) Proposed $\left| 3N_p - N_r \right|$ winding design.

Changes Made:

We have updated the manuscript by adding the evaluation of unbalanced magnetic force (See Part D of Section IV).

5. **Reviewer's comment:**

Fig. 2(b) shows a classical 4-pole winding of a conventional machine with overlapping end windings – the latter is a serious disadvantage compared to the normal tooth winding machine in terms of copper loss and overall machine length. The difference in copper loss between the proposed 12/11/2 and the other VRM models (or at least the 12/11/8) should be highlighted in the paper and not just the core losses as in Fig. 11.

Response-21:

Thanks for your concern. In the original manuscript, we have included the influence of increased end copper loss in efficiency evaluation. The results of copper loss in eight optimal models are show in Table X, while the core loss and efficiency curves are provided in Fig. 11 and Fig. 12 below. It can be seen, because of increased end copper loss, the efficiency of our proposed 12/11/2 design becomes slightly lower than 12/11/8 case, although the torque density is significantly improved by 75%. We include this statement in the conclusion part to discuss the influence of increase end copper loss. Meanwhile, it should be pointed out, the influence of end copper loss is closely related to the ratio of stack length and outer dimension. When the machine design has increased ratio of stack length and outer dimension, the influence of end copper loss becomes less, and our proposed technique becomes more advantageous in both torque density and efficiency.

TABLE X

COPPER LOSS UNDER RATED CURRENT

	Traditional $\|N_p\text{-}N_r\|$ winding				Proposed $\|3N_p\text{-}N_r\|$ winding			
N_{slot}	12	12	12	12	12	12	12	12
N_r	11	10	8	7	11	10	8	7
PPN_a	8	7	5	4	2	1	1	2
P_{Cu}(W)	97.89	114.03	108.92	110.21	142.98	201.92	231.7	97.51

Fig. 11.   Core loss. (a) VRMs with traditional $\|N_p\text{-}N_r\|$ winding. (b) VRMs with proposed $\|3N_p\text{-}N_r\|$ winding.
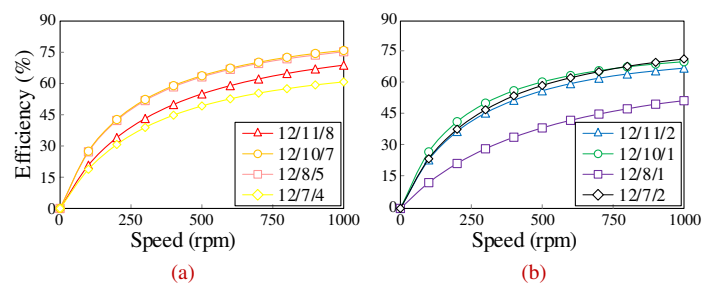
Fig. 12.   Efficiency. (a) VRMs with traditional $\|N_p\text{-}N_r\|$ winding. (b) VRMs with proposed $\|3N_p\text{-}N_r\|$ winding.

Changes Made:

We have updated the manuscript by adding the data of copper loss of eight optimal models (See Part C of Section IV), and the influence of copper loss in efficiency (Conclusion part).

6. **Reviewer's comment:**

A photo of the end winding layout of the experimental machine will be very informative for the reader to see how this looks like, because it is not an easy winding, and with every second slot fully packed and every second slot semi open.

Response-22:

Thanks for your suggestion. The winding layout of the experimental prototype is presented as follows. The AC armature windings and the DC field windings are marked in the picture.
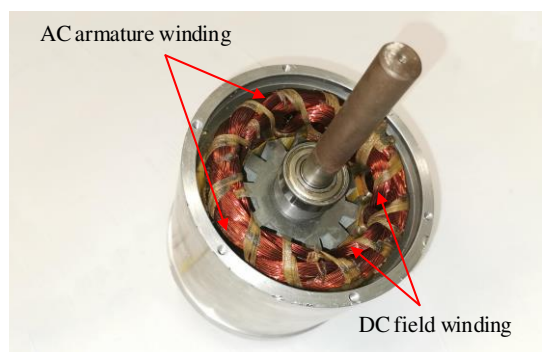
Fig. 16(c).   Winding layout of the prototype.

Changes Made:

We have updated the manuscript by adding the winding layout of the prototype. (See Fig. 16(c) in Section V).

7. **Reviewer's comment:**

In (3), mustn't "Fdc" be "F1" as shown in Fig. 3?

Response-23:

Thanks for pointing it out. We are sorry for this typo, the correct symbol should be F_{dc}.

Changes Made:

We have updated the manuscript by correcting the typo in Fig. 3 (See Part B of Section II).

8. **Reviewer's comment:**

The authors must explain to the reader why in Fig. 6(a) the flux density B(3,-1) [blue] is a factor say 1.4 larger than B(1,-1) [red], but in Table IV it is almost the other way round for the 12/11 machine?

Response-24:

Thanks for pointing it out. We are sorry for this mistake in Fig. 6 as the main working harmonics are marked by mistake in 12/11 case. The Fig. 6(a) has been corrected.

Changes Made:

We have updated the manuscript by correcting the mistake in Fig. 6 (See Part D of Section II).

9. **Reviewer's comment:**

Why is the machine tested at 900 r/min? Does the proposed machine operate at a different speed versus frequency? The authors must for the reader explains the difference in frequency (if any) of their new proposed winding compared to the 12/11/8 and also to, say, the classical well-known 12/10 full DC tooth winding that operates at 300 r/min at 50 Hz (if I am right).

Response-25:

Thanks for your questions. The prototype is tested at 900 rpm as it is the rated speed in this design. The proposed machine does not operate at a different speed versus frequency. The frequency can be determined by the following equation.

$$f = \frac{np}{60}$$

where n is the rotation speed, p is the rotor teeth number, and f is the frequency. The frequency is only determined by the rotation speed and rotor teeth number. And it is independent of AC armature winding design. Therefore, compared with traditional 12/11/8 design, the 12/11/2 design has the same operating frequency under the same speed.

The frequency of proposed machine is also independent of DC field winding design. Therefore, the above-mentioned equation can be used for both the proposed machine and classical well-known 12/10 full DC tooth winding design, no matter which DC field winding design is used.

10. **Reviewer's comment:**

The authors found a remarkable 75% increase in torque (almost doubling) of their proposed machine compared to the 12/11/8 machine. However, for the reader, the authors must state or comment on how the torque density of their 12/11/2 machine compares to the classical well-known 12/10 full DC tooth winding machine (i.e., with tooth DC coils).

Response-26:

Thanks for your concern. We made a comparison between the proposed 12/11/2 machine and the conventional 12/10 full DC tooth winding machine, which are presented as follow. The traditional machine is optimized under the same current density, rotation speed, airgap length, maximum diameter and stack length with the proposed machine. The torque production, copper loss, core loss and efficiency of two models are summarized as follow.
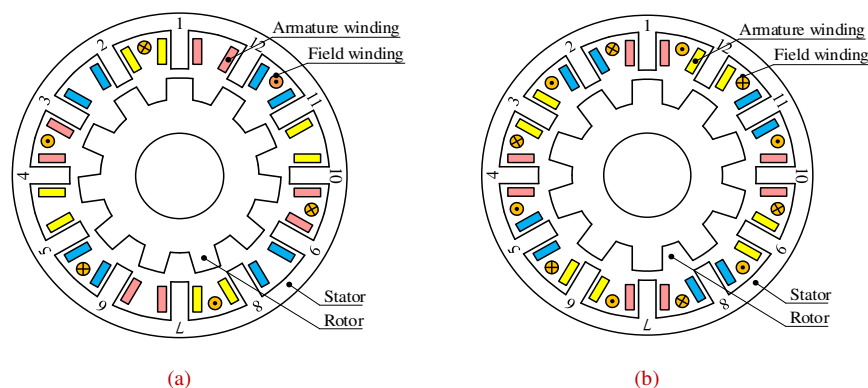

Fig. 25. (a) The proposed 12/11/2 machine. (b) the conventional 12/10 full DC tooth winding machine.

TABLE XI

COMPARISON BETWEEN THE PROPOSED 12/11/2 DESIGN AND 12/10 FULL DC TOOTH WINDING MACHINE

Machine type	Average torque (Nm)	Torque ripple (%)	Copper loss (W)	Core loss (W)	Efficiency (%)
Proposed 12/11/2 design	4.30	16.7%	142.98	65.0	66.1
12/10 full DC tooth winding design	3.88	12.5%	164.18	35.2	64.9

Compare with the traditional machine, the proposed 12/11/2 machine have 10% higher output torque. Besides, with the DC coil number reduced by half, the proposed machine has lower copper loss. The core loss in the proposed machine is relatively higher due to the influence of high-order harmonics. In conclusion, the proposed 12/11/2 machine shows higher torque production, lower copper loss and higher efficiency, compared with the conventional 12/10 full DC tooth winding machine.

This paper focuses on the AC armature winding design methods for VRM with DC coils across two stator teeth, the comparison against traditional full DC coil layout is not the key point for this manuscript, and therefore not included considering page limit.

Reply to Reviewer 4:

1. **Reviewer's comment:**

It is mentioned in the abstract as well in the conclusion that the torque density can be improved by 75.6%. However, this improvement only happens in 12/11 case. Other stator/rotor slot combination are not discussed in detail.

Response-27:

Thanks for pulling up this question. The torque performances of 8 optimal designs are presented in the Table IX below. It is shown the torque improvement occurs not only in the 12/11/2 case, but also in the 12/7/2 case. However, the improvement is not very attractive in the 12/10/1 and 12/8/1 cases. The reason behind this phenomenon is provided as follow.

TABLE IX
TORQUE PERFORMANCE OF OPTIMAL MODELS

	N_{slot}	N_r	PPN_a	T_{avg} (Nm)	Ripple
Traditional $\|N_p - N_r\|$ winding	12	11	8	2.45 Nm	19.8%
	12	10	7	4.19 Nm	69.2%
	12	8	5	3.96 Nm	38.4%
	12	7	4	2.24 Nm	33.2%
Proposed $\|3N_p - N_r\|$ winding	12	11	2	4.30 Nm	16.7%
	12	10	1	4.03 Nm	80.8%
	12	8	1	3.01 Nm	72.0%
	12	7	2	3.36 Nm	8.9%

According to the analysis on open-circuit back EMF (can be referred to Response-11, or Part E of Section II in the revised manuscript), the open-circuit back EMF can be improved in all the cases when the proposed winding design is used. However, the torque production is not in direct proportion to back EMF when the core saturation is considered. Because the 1-pole-pair armature field in the 12/10/1 and 12/8/1 cases is much easier to be saturated due to longer magnetic circuit,

compared to that of 2-pole-pair armature field in the 12/11/2 and 12/7/2 cases (as shown in Fig. 9 below), the torque production of the proposed winding design in 12/10/1 and 12/8/1 cases are limited by core saturation effect especially in stator yoke. Therefore, the proposed winding design method is recommended for 12/11/2 and 12/7 /2 cases.

Traditional |N$_\text{P}$-N$_\text{r}$| Winding   **Proposed |3N$_\text{P}$-N$_\text{r}$| Winding**

(a)

(b)

(c)

(d)
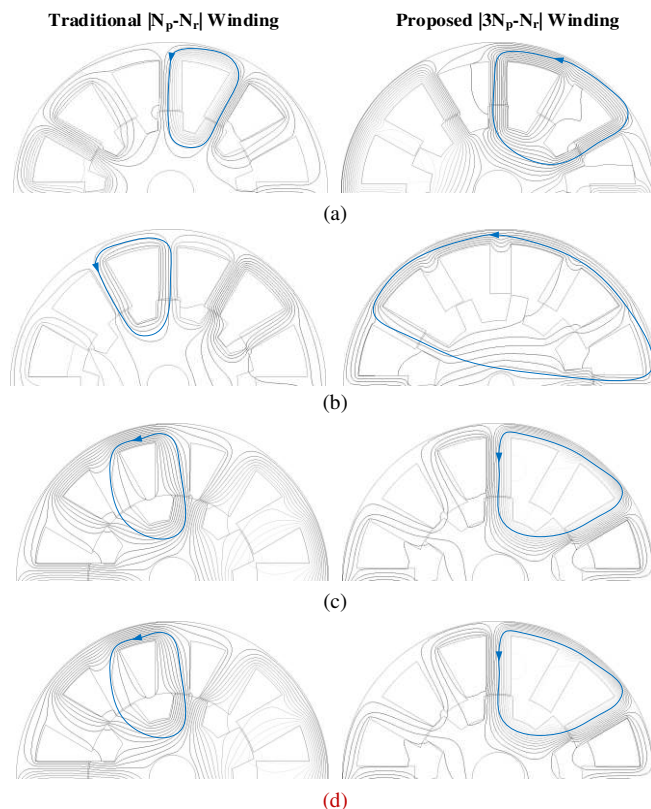
Fig. 9.   Flux linkage distribution (a) 11 rotor poles. (b) 10 rotor poles. (c) 8 rotor poles. (d) 7 rotor poles.

Changes Made:

The reasons why the improvement is more outstanding in 12/11/2 and 12/7/2 cases are discussed. (See Part A of Section IV).

2. **Reviewer's comment:**

Fig. 6 and Table IV shows working harmonic however their amplitudes do not seem to be the same. Please check it again and add an explanation as except the Fig. 6 (a), other working harmonic amplitudes are lower with the proposed technique. Also, please discuss further in detail the main working harmonic components ratio in the proposed winding as to how it is advantageous? Also please add a short paragraph comparing the proposed topology with the DC field coils wound on every tooth as it is mentioned that the working flux harmonic ratio becomes 3 in this case and the proposed technique is not advantageous.

Response-28:

Thanks for your suggestion. We are sorry for this mistake in Fig. 6(a) as the main working harmonics are marked by mistake in 12/11 case. The Fig. 6(a) has been corrected.

As for the working harmonic components ratio, the back EMF produced by each working harmonic can be expressed as

$$E_{phn} = \frac{4.44 DLT_{ph}}{60} \left(B_n k_{wn} \omega_n \right)$$

where D is the diameter of the airgap circumference, L is the stack length, T_{ph} is the number of turns in a phase, E_{phn} is the amplitude of back EMF contributed by nth harmonic, B_n is the amplitude of nth harmonic, ω_n is the rotation speed of nth harmonic, and k_{wn} is the winding factor of nth harmonic, which can be expressed as

$$k_{wn} = k_{pn} k_{dn}$$

where k_{pn} is the pitch factor of nth harmonic and k_{dn} is the distribution factor of nth harmonic. The back EMF produced by each harmonic and their amplitude, rotation speed and winding factor are calculated and listed in Table V and Table VI, using 12/11/8 and 12/11/2 as the examples. The harmonics with the order higher than 32 are neglected as contributions are too small.

TABLE V

OPEN-CIRCUIT BACK EMF CONTRIBUTION FROM DIFFERENT HARMONICS IN 12/11/8 MODEL

Order	(n,k)	B_n (T)	ω_n	k_{pn}	k_{dn}	k_{wn}	$B_n\omega_n k_{wn}$	$\sum B_n\omega_n k_{wn}$
2	(3,-1)	0.1093	$11\omega_{me}/2$	0.5	0	0	0	
4	(5,-1)	0.0755	$11\omega_{me}/4$	0.866	1	0.866	$0.1798\omega_{me}$	
8	(1,-1)	0.1419	$11\omega_{me}/8$	0.866	1	0.866	$0.1690\omega_{me}$	
10	(7,-1)	0.0376	$11\omega_{me}/10$	0.5	0	0	0	
14	(-1,-1)	0.1433	$11\omega_{me}/14$	-0.5	0	0	0	
16	(9,-1)	0.007	$11\omega_{me}/16$	-0.866	1	-0.866	$-0.004\omega_{me}$	$0.3072\omega_{me}$
20	(-3,-1)	0.1096	$11\omega_{me}/20$	-0.866	1	-0.866	$-0.0522\omega_{me}$	
22	(11,-1)	0.0114	$11\omega_{me}/22$	-0.5	0	0	0	
26	(-5,-1)	0.0704	$11\omega_{me}/26$	0.5	0	0	0	
28	(13,-1)	0.0198	$11\omega_{me}/28$	0.866	1	0.866	$0.0067\omega_{me}$	
32	(-7,-1)	0.0370	$11\omega_{me}/32$	0.866	1	0.866	$0.0110\omega_{me}$	

TABLE VI

OPEN-CIRCUIT BACK EMF CONTRIBUTION FROM DIFFERENT HARMONICS IN 12/11/2 MODEL

Order	(n,k)	B_n (T)	ω_n	k_{pn}	k_{dn}	k_{wn}	$B_n\omega_n k_{wn}$	$\sum B_n\omega_n k_{wn}$
2	(3,-1)	0.1093	$11\omega_{me}/2$	1	1	1	$0.6010\omega_{me}$	
4	(5,-1)	0.0755	$11\omega_{me}/4$	0	0	0	0	
8	(1,-1)	0.1419	$11\omega_{me}/8$	0	0	0	0	
10	(7,-1)	0.0376	$11\omega_{me}/10$	1	1	1	$0.0413\omega_{me}$	
14	(-1,-1)	0.1433	$11\omega_{me}/14$	-1	1	-1	$-0.1125\omega_{me}$	
16	(9,-1)	0.007	$11\omega_{me}/16$	0	0	0	0	$0.5573\omega_{me}$
20	(-3,-1)	0.1096	$11\omega_{me}/20$	0	0	0	0	
22	(11,-1)	0.0114	$11\omega_{me}/22$	-1	1	-1	$-0.0057\omega_{me}$	
26	(-5,-1)	0.0704	$11\omega_{me}/26$	1	1	1	$0.0298\omega_{me}$	
28	(13,-1)	0.0198	$11\omega_{me}/28$	0	0	0	0	
32	(-7,-1)	0.0370	$11\omega_{me}/32$	0	0	0	0	

Although the amplitude of each air-gap flux harmonic of the traditional 12/11/8 design and proposed 12/11/2 design are the same, the corresponding winding factors are different. The main working harmonics are 4-pole-pair and 8-pole-pair for the traditional design, while that is 2-pole-pair for the proposed one. Although the amplitude of 2-pole-pair harmonic is relatively lower, the rotation speed is much higher. Therefore, the open-circuit back EMF of the proposed winding design is higher than the traditional counterpart. The analytical ratio of back EMF between two winding designs is 1.814, which agrees with the FEA result of 1.934 (error = 6.86%).

A similar analysis has been applied to other six models. And the relevant data are presented in Appendix in the end of this response letter.

In general, according to the flux modulation theory, the rotation speed of modulated harmonic is in inverse proportion to harmonic order. The lower order of working harmonic order is, the higher rotation speed can be achieved, and thus higher back EMF and torque production can be obtained. This is the motivation of the proposed novel winding design method to improve torque density.

As requested by the reviewer, we perform a MMF comparison between two DC layouts (across two stator teeth and fully wound on each stator tooth, respectively). In the traditional full DC coil design, the main working harmonic ratio is 3 and the detailed derivation is proved as follows.
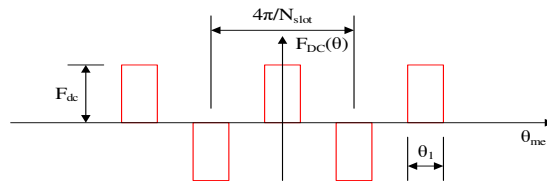
Fig. 26.　MMF of DC field coils fully wound on each stator tooth.

The MMF of DC field coils ($F_{DC}(\theta)$) with respective to mechanical angle can be expressed as

$$F_{DC}(\theta) = \sum_{n=1}^{+\infty} F_n \cos\left(n\frac{N_{slot}}{2}\theta\right)$$

where N_{slot} is the number of slots and F_n is the nth harmonic of MMF of DC field coils. F_n can be further expressed as

$$F_n = \frac{N_{slot}}{2\pi} \int_{-\frac{4\pi}{N_{slot}}}^{\frac{4\pi}{N_{slot}}} F_{DC}(\theta) \cos\left(n\frac{N_{slot}}{2}\theta\right) d\theta$$

$$= \frac{N_{slot}}{\pi} \left[\int_0^{\frac{\theta_1}{2}} F_{dc} \cos\left(n\frac{N_{slot}}{2}\theta\right) d\theta - \int_{\frac{2\pi}{N_{slot}}-\frac{\theta_1}{2}}^{\frac{2\pi}{N_{slot}}} F_{dc} \cos\left(n\frac{N_{slot}}{2}\theta\right) d\theta\right]$$

$$= \frac{N_{slot}}{\pi} \left[\frac{2F_{dc}}{nN_{slot}} \sin\left(n\frac{N_{slot}}{2}\theta\right)\Big|_0^{\frac{\theta_1}{2}} - \frac{2F_{dc}}{nN_{slot}} \sin\left(n\frac{N_{slot}}{2}\theta\right)\Big|_{\frac{2\pi}{N_{slot}}-\frac{\theta_1}{2}}^{\frac{2\pi}{N_{slot}}}\right]$$

$$= \frac{2F_{dc}}{n\pi} \left[\sin\left(n\frac{N_{slot}}{4}\theta_1\right) - \sin(n\pi) + \sin\left(n\pi - n\frac{N_{slot}}{4}\theta_1\right)\right]$$

Similarly, suppose the stator tooth has the same angular size with slot open, which means $\theta_1 \approx \frac{\pi}{N_{slot}}$, the amplitude ratio between working harmonics modulated by fundamental harmonic and 3rd harmonic can be deduced as follows.

$$\frac{|B_{(1,-1)}|}{|B_{(3,-1)}|} = \frac{|F_1 P_{-1}|}{|F_3 P_{-1}|} = \frac{|F_1|}{|F_3|} = \frac{\left|\frac{2F_{dc}}{\pi}\left[\sin\left(\frac{N_{slot}}{4}\theta_1\right) - \sin(\pi) + \sin\left(\pi - \frac{N_{slot}}{4}\theta_1\right)\right]\right|}{\left|\frac{2F_{dc}}{3\pi}\left[\sin\left(3\frac{N_{slot}}{4}\theta_1\right) - \sin(3\pi) + \sin\left(3\pi - 3\frac{N_{slot}}{4}\theta_1\right)\right]\right|} \approx 3$$

Therefore, if the DC field coils are fully wound on each stator tooth, the amplitude of 3rd working harmonic is much lower than the fundamental harmonic. Hence, the proposed winding design method is not advantageous in this case.

Changes Made:

We have updated the manuscript by correcting the mistake of Fig. 6(a) (See Part D of Section II). The main working harmonic components ratio in the proposed and traditional winding is analyzed in detail. And the mechanism how the proposed technique is advantageous is provided. (See Part E of Section II). A short paragraph comparing the proposed topology with the DC field coils wound on every tooth is highlighted. (See Part C of Section II)

3. **Reviewer's comment:**

    Page 5, right column, line 46, a typo "sdis". Please correct it..

    Response-29:

    Thanks for your advice. Sorry for this typo and it has been corrected in the updated manuscript.

    Changes Made:

    We have updated the manuscript by correcting the typo. (See Part A of Section IV)

4. **Reviewer's comment:**

    Section 4, subsection B: Higher THD% require further explanation.

    Response-30:

    Thanks for your advice. As is presented in Fig. 10 below, the main reason for high THD in 12/10 and 12/8 cases is that there are high even harmonics in the open-circuit back EMF. By contrary, in 12/11 and 12/7 cases, the even harmonics are almost zero. The reason for this difference is that the winding factor of 12/11 and 12/7 cases is zero in terms of even harmonic in back EMF. Therefore, the THDs of 12/10 and 12/8 cases are relatively higher than 12/11 and 12/7 cases.

(a)

(b)

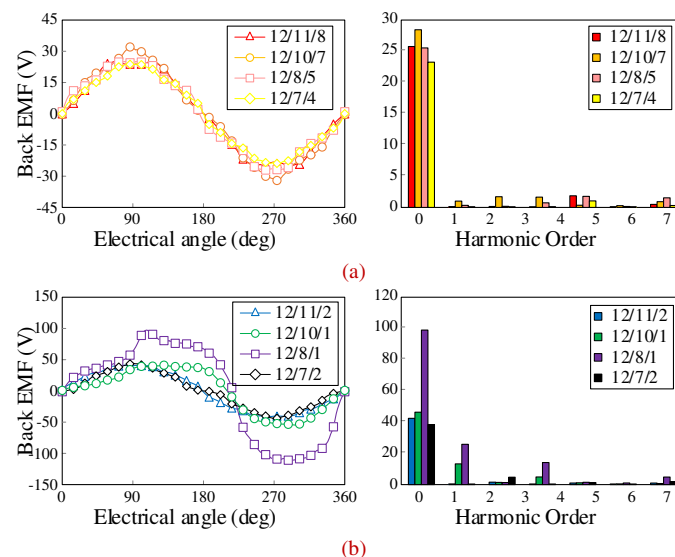Fig. 10.   Back EMF and harmonics (a) The traditional $\left| N_p \text{-} N_r \right|$ winding. (b) The proposed $\left| 3N_p \text{-} N_r \right|$ winding.

Changes Made:

We have added the reason for high THD in 12/10 and 12/8 cases. (See Part A of Section IV)

1
2
3
4
5
6
7
8
9
10
11
12
13
14
15
16
17
18
19
20
21
22
23
24
25
26
27
28
29
30
31
32
33
34
35
36
37
38
39
40
41
42
43
44
45
46
47
48
49
50
51
52
53
54
55
56
57
58
59
60

Appendix:

OPEN-CIRCUIT BACK EMF CONTRIBUTION FROM DIFFERENT HARMONICS IN 12/10/7 MODEL

Order	(n,k)	B_n (T)	ω_n	k_{pn}	k_{dn}	k_{wn}	$B_n\omega_n k_{wn}$	$\sum B_n\omega_n k_{wn}$
1	(3,-1)	0.1089	$10\omega_{me}/1$	0.2588	0.2588	0.0670	$0.0802\omega_{me}$	
5	(5,-1)	0.0775	$10\omega_{me}/5$	0.9659	0.9659	0.9330	$0.1590\omega_{me}$	
7	(1,-1)	0.1436	$10\omega_{me}/7$	0.9659	0.9659	0.9330	$0.2106\omega_{me}$	
11	(7,-1)	0.0401	$10\omega_{me}/11$	0.2588	0.2588	0.0670	$0.0027\omega_{me}$	
13	(-1,-1)	0.1442	$10\omega_{me}/13$	-0.2588	0.2588	-0.0670	$-0.0082\omega_{me}$	
17	(9,-1)	0.0191	$10\omega_{me}/17$	-0.9659	0.9659	-0.9330	$-0.0116\omega_{me}$	$0.3921\omega_{me}$
19	(-3,-1)	0.1116	$10\omega_{me}/19$	-0.9659	0.9659	-0.9330	$-0.0603\omega_{me}$	
23	(11,-1)	0.0238	$10\omega_{me}/23$	-0.2588	0.2588	-0.0670	$-0.0008\omega_{me}$	
25	(-5,-1)	0.0730	$10\omega_{me}/25$	0.2588	0.2588	0.0670	$0.0022\omega_{me}$	
29	(13,-1)	0.0264	$10\omega_{me}/29$	0.9659	0.9659	0.9330	$0.0094\omega_{me}$	
31	(-7,-1)	0.0413	$10\omega_{me}/31$	0.9659	0.9659	0.9330	$0.0137\omega_{me}$	

OPEN-CIRCUIT BACK EMF CONTRIBUTION FROM DIFFERENT HARMONICS IN 12/10/1 MODEL

Order	(n,k)	B_n (T)	ω_n	k_{pn}	k_{dn}	k_{wn}	$B_n\omega_n k_{wn}$	$\sum B_n\omega_n k_{wn}$
1	(3,-1)	0.1089	$10\omega_{me}/1$	1	0.9659	0.9659	$1.1566\omega_{me}$	
5	(5,-1)	0.0775	$10\omega_{me}/5$	1	0.2588	0.2588	$0.0441\omega_{me}$	
7	(1,-1)	0.1436	$10\omega_{me}/7$	-1	0.2588	-0.2588	$-0.0584\omega_{me}$	
11	(7,-1)	0.0401	$10\omega_{me}/11$	-1	0.9659	-0.9659	$-0.0387\omega_{me}$	
13	(-1,-1)	0.1442	$10\omega_{me}/13$	1	0.9659	0.9659	$0.1178\omega_{me}$	
17	(9,-1)	0.0191	$10\omega_{me}/17$	1	0.2588	0.2588	$0.0032\omega_{me}$	$1.2309\omega_{me}$
19	(-3,-1)	0.1116	$10\omega_{me}/19$	-1	0.2588	-0.2588	$-0.0167\omega_{me}$	
23	(11,-1)	0.0238	$10\omega_{me}/23$	-1	0.9659	-0.9659	$-0.0110\omega_{me}$	
25	(-5,-1)	0.0730	$10\omega_{me}/25$	1	0.9659	0.9659	$0.0310\omega_{me}$	
29	(13,-1)	0.0264	$10\omega_{me}/29$	1	0.2588	0.2588	$0.0026\omega_{me}$	
31	(-7,-1)	0.0413	$10\omega_{me}/31$	-1	0.2588	-0.2588	$-0.0038\omega_{me}$	

OPEN-CIRCUIT BACK EMF CONTRIBUTION FROM DIFFERENT HARMONICS IN 12/8/5 MODEL

Order	(n,k)	B_n (T)	ω_n	k_{pn}	k_{dn}	k_{wn}	$B_n\omega_n k_{wn}$	$\sum B_n\omega_n k_{wn}$
1	(3,-1)	0.1353	$8\omega_{me}/1$	0.2588	0.2588	0.0670	$0.0997\omega_{me}$	
5	(1,-1)	0.1506	$8\omega_{me}/5$	0.9659	0.9659	0.9330	$0.3092\omega_{me}$	
7	(5,-1)	0.1157	$8\omega_{me}/7$	0.9659	0.9659	0.9330	$0.1696\omega_{me}$	
11	(-1,-1)	0.1295	$8\omega_{me}/11$	0.2588	0.2588	0.0670	$0.0087\omega_{me}$	
13	(7,-1)	0.0883	$8\omega_{me}/13$	-0.2588	0.2588	-0.0670	$-0.0050\omega_{me}$	
17	(-3,-1)	0.0821	$8\omega_{me}/17$	-0.9659	0.9659	-0.9330	$-0.0496\omega_{me}$	$0.4896\omega_{me}$
19	(9,-1)	0.0602	$8\omega_{me}/19$	-0.9659	0.9659	-0.9330	$-0.0325\omega_{me}$	
23	(-5,-1)	0.0363	$8\omega_{me}/23$	-0.2588	0.2588	-0.0670	$-0.0012\omega_{me}$	
25	(11,-1)	0.0255	$8\omega_{me}/25$	0.2588	0.2588	0.0670	$0.0008\omega_{me}$	
29	(-7,-1)	0.0015	$8\omega_{me}/29$	0.9659	0.9659	0.9330	$0.0005\omega_{me}$	
31	(13,-1)	0.0036	$8\omega_{me}/31$	0.9659	0.9659	0.9330	$0.0012\omega_{me}$	

1
2
3
4
5
6
7
8
9
10
11
12
13
14
15
16
17
18
19
20

OPEN-CIRCUIT BACK EMF CONTRIBUTION FROM DIFFERENT HARMONICS IN 12/8/1 MODEL

Order	(n,k)	B_n (T)	ω_n	k_{pn}	k_{dn}	k_{wn}	$B_n\omega_n k_{wn}$	$\Sigma B_n\omega_n k_{wn}$
1	(3,-1)	0.1353	$8\omega_{me}/1$	1	0.9659	0.9659	$1.4373\omega_{me}$	
5	(1,-1)	0.1506	$8\omega_{me}/5$	1	0.2588	0.2588	$0.0858\omega_{me}$	
7	(5,-1)	0.1157	$8\omega_{me}/7$	-1	0.2588	-0.2588	$-0.0470\omega_{me}$	
11	(-1,-1)	0.1295	$8\omega_{me}/11$	-1	0.9659	-0.9659	$-0.1251\omega_{me}$	
13	(7,-1)	0.0883	$8\omega_{me}/13$	1	0.9659	0.9659	$0.0721\omega_{me}$	
17	(-3,-1)	0.0821	$8\omega_{me}/17$	1	0.2588	0.2588	$0.0138\omega_{me}$	$1.4212\omega_{me}$
19	(9,-1)	0.0602	$8\omega_{me}/19$	-1	0.2588	-0.2588	$-0.0090\omega_{me}$	
23	(-5,-1)	0.0363	$8\omega_{me}/23$	-1	0.9659	-0.9659	$-0.0168\omega_{me}$	
25	(11,-1)	0.0255	$8\omega_{me}/25$	1	0.9659	0.9659	$0.0108\omega_{me}$	
29	(-7,-1)	0.0015	$8\omega_{me}/29$	1	0.2588	0.2588	$0.0002\omega_{me}$	
31	(13,-1)	0.0036	$8\omega_{me}/31$	-1	0.2588	-0.2588	$-0.0003\omega_{me}$	

21
22
23
24

OPEN-CIRCUIT BACK EMF CONTRIBUTION FROM DIFFERENT HARMONICS IN 12/7/4 MODEL

Order	(n,k)	B_n (T)	ω_n	k_{pn}	k_{dn}	k_{wn}	$B_n\omega_n k_{wn}$	$\Sigma B_n\omega_n k_{wn}$
2	(3,-1)	0.0893	$7\omega_{me}/2$	0.5	0	0	0	
4	(1,-1)	0.1236	$7\omega_{me}/4$	0.8660	1	0.8660	$0.2944\omega_{me}$	
8	(5,-1)	0.0618	$7\omega_{me}/8$	0.8660	1	0.8660	$0.0736\omega_{me}$	
10	(-1,-1)	0.1198	$7\omega_{me}/10$	0.5	0	0	0	
14	(7,-1)	0.0293	$7\omega_{me}/14$	-0.5	0	0	0	
16	(-3,-1)	0.0905	$7\omega_{me}/16$	-0.8660	1	-0.8660	$-0.0539\omega_{me}$	$0.3225\omega_{me}$
20	(9,-1)	0.0131	$7\omega_{me}/20$	-0.8660	1	-0.8660	$-0.0062\omega_{me}$	
22	(-5,-1)	0.0578	$7\omega_{me}/22$	-0.5	0	0	0	
26	(11,-1)	0.0211	$7\omega_{me}/26$	0.5	0	0	0	
28	(-7,-1)	0.0298	$7\omega_{me}/28$	0.8660	1	0.8660	$0.0102\omega_{me}$	
32	(13,-1)	0.0287	$7\omega_{me}/32$	0.8660	1	0.8660	$0.0085\omega_{me}$	

25
26
27
28
29
30
31
32
33
34
35
36
37
38
39
40
41
42
43
44

OPEN-CIRCUIT BACK EMF CONTRIBUTION FROM DIFFERENT HARMONICS IN 12/7/2 MODEL

Order	(n,k)	B_n (T)	ω_n	k_{pn}	k_{dn}	k_{wn}	$B_n\omega_n k_{wn}$	$\Sigma B_n\omega_n k_{wn}$
2	(3,-1)	0.0893	$7\omega_{me}/2$	1	1	1	$0.4914\omega_{me}$	
4	(1,-1)	0.1236	$7\omega_{me}/4$	0	0	0	0	
8	(5,-1)	0.0618	$7\omega_{me}/8$	0	0	0	0	
10	(-1,-1)	0.1198	$7\omega_{me}/10$	1	1	1	$0.1317\omega_{me}$	
14	(7,-1)	0.0293	$7\omega_{me}/14$	-1	1	-1	$-0.0231\omega_{me}$	
16	(-3,-1)	0.0905	$7\omega_{me}/16$	0	0	0	0	$0.5755\omega_{me}$
20	(9,-1)	0.0131	$7\omega_{me}/20$	0	0	0	0	
22	(-5,-1)	0.0578	$7\omega_{me}/22$	-1	1	-1	$-0.0289\omega_{me}$	
26	(11,-1)	0.0211	$7\omega_{me}/26$	1	1	1	$0.0089\omega_{me}$	
28	(-7,-1)	0.0298	$7\omega_{me}/28$	0	0	0	0	
32	(13,-1)	0.0287	$7\omega_{me}/32$	0	0	0	0	

45
46
47
48
49
50
51
52
53
54
55
56
57
58
59
60